Plant, Cell & Environment

WILEY

Plant, Cell & Environment

ORIGINAL ARTICLE

Integrated Metabolomic, Lipidomic and Proteomic Analysis Define the Metabolic Changes Occurring in Curled Areas in Leaves With Leaf Peach Curl Disease

María Angelina Novello[1] | Claudia Anabel Bustamante[1] | Laura Andrea Svetaz[1] | Camila Goldy[1] | Gabriel Hugo Valentini[2] | María Fabiana Drincovich[1] | Yariv Brotman[3] | Alisdair R. Fernie[4] | María Valeria Lara[1]

[1]Centro de Estudios Fotosintéticos y Bioquímicos (CEFOBI), Facultad de Ciencias Bioquímicas y Farmacéuticas, Universidad Nacional de Rosario, Rosario, Argentina | [2]Estación Experimental San Pedro, Instituto Nacional de Tecnología Agropecuaria (INTA), San Pedro, Argentina | [3]School of Plant Sciences and Food Security, Tel Aviv University, Tel Aviv, Israel | [4]Max-Planck-Institut für Molekulare Pflanzenphysiologie, Potsdam-Golm, Germany

Correspondence: María Valeria Lara (lara@cefobi-conicet.gov.ar)

Received: 8 March 2024 | **Revised:** 27 August 2024 | **Accepted:** 27 September 2024

Funding: This work was supported by Agencia Nacional de Promoción Científica y Tecnológica (PICT 2016-0819).

Keywords: defence | phytohormones | *Prunus persica* | *Taphrina deformans*

ABSTRACT

Peach Leaf Curl Disease, caused by *Taphrina deformans*, is characterized by reddish hypertrophic and hyperplasic leaf areas. To comprehend the biochemical imbalances caused by the fungus, dissected symptomatic (C) and asymptomatic areas (N) from leaves with increasing disease extension were analyzed by an integrated approach including metabolomics, lipidomics, proteomics, and complementary biochemical techniques. Drastic metabolic differences were identified in C areas with respect to either N areas or healthy leaves, including altered chloroplastic functioning and composition, which differs from the typical senescence process. In C areas, alteration in redox-homoeostasis proteins and in triacylglycerols content, peroxidation and double bond index were observed. Proteomic data revealed induction of host enzymes involved in auxin and jasmonate biosynthesis and an upregulation of phenylpropanoid and mevalonate pathways and downregulation of the plastidic methylerythritol phosphate route. Amino acid pools were affected, with upregulation of proteins involved in asparagine synthesis. Curled areas exhibited a metabolic shift towards functioning as a sink tissue importing sugars, probably from N areas, and producing energy through fermentation and respiration and reductive power via the pentose phosphate route. Identifying the metabolic disturbances leading to disease symptoms is a key step in designing strategies to prevent or delay the progression of the disease.

1 | Introduction

Prunus persica L. Batsch is a climacteric stone fruit that holds an important significance in agriculture, with a global production of more than 25 million tonnes per year. Peach is also relevant to human health as it is a notable source of phytochemicals such as phenolics, cyanogenic glucosides and phytoestrogens (Lara et al. 2020). As all crops, peach orchards

Abbreviations: AGP, ADP-glucose pyrophosphorylase; ADH, alcohol dehydrogenase; β-CAS, L-3-cyanoalanine synthase 1; AOC, allene-oxide cyclase; DAG, diacylglycerol; CW, cell wall; DAP, differentially abundant protein; DGDG, digalactosyldiacylglycerol; DBI, double bond index; FC, fold change; IPP, isopentenyl pyrophosphate; PLCD, peach leaf curl disease; LSU, large subunit; LHCII, light harvesting complex II; LOX, lipoxygenase; MEP, methylerythritol phosphate; MGDG, monogalactosyldiacylglycerol; NMR, neomenthol dehydrogenase; OPPP, oxidative pentose phosphate pathway; PR, pathogenesis related; PC, phosphatidylcholine; PEPC, phospho*enol*pyruvate carboxylase; PSII, photosystem II; PC, principal component; PCA, PC analysis; PE, phosphatidylethanolamine; PG, phosphatidylglycerol; PI, phosphatidylinositol; PDH, pyruvate dehydrogenase; TAG, triacylglycerol; TRX, thioredoxin reductases; TCAC, tricarboxylic acid cycle; SQDG, sulfoquinovosyl diacylglycerol.

María Angelina Novello and Claudia Anabel Bustamante contributed equally to this study.

are threatened by different pathogens. Peach leaf curl disease (PLCD) is caused by the biotrophic fungus *Taphrina deformans* that infects peach, almond and nectarines in most of the cultivated areas (Cimen and Ertugrul 2007). The severity of leaf damage is assessed based on the Ritchie, (1981) scale. Healthy leaves are assigned as grade zero while grades one to nine include leaves with different extent of the symptoms. The incidence of PLCD is directly linked to climatic factors. Under low temperature, rainy seasons and high relative humidity, impact can be up to 89% for shoots and 50% for fruits (Rossi et al. 2006, 2007). PLCD affects fruit yield and quality and it compromises the overall tree health and strength. Infected trees are more vulnerable to other pathogens and environmental stresses conducting to indirect but devastating economic losses (Agrios 2005).

The initial signs of the pathology appear in late winter or early spring. *T. deformans* ascospores undergo asexual budding to produce conidia, initiating the infection by generating a germination tube that forms a binucleate hypha that penetrates the tissue through stomata or the cuticle and young leaves start to exhibit chlorotic regions (Giordani, Padula, and Radice 2013). The mycelium develops within the apoplastic space, colonizing the tissue. Some hyphae penetrate deeper into the tissue, while others spread between the epidermis and the parenchyma. As *T. deformans* grows, it stimulates cells to excessively divide and elongate causing tissue thickening and deformation. This excessively cell enlargement could be due to the presence of auxins and cytokinins; however, it is yet unclear if *T. deformans* itself synthetizes the hormones or if it triggers host cells to produce them (Yamada et al. 1990). The disease progresses as the chlorotic leaves gain a reddish coloration that darken and turn purplish by the accumulation of pigments, while the tissue continues to enlarge. This leads to leaf curl inward and downward giving the distinctive distorted aspect (Fonseca and Rodrigues 2011). Subsequently, mycelium undergoes meiosis to produce ascospores enclosed within asci, which break and penetrate the cuticle to the exterior. Finally, as the leaves start to fall causing a massive defoliation, ascospores can disperse and initiate a new cycle of infection (Agrios 2005; Rossi and Languasco 2007).

The mycelium modifies the anatomy of cells from infected leaves (Giordani, Padula, and Radice 2013). The fungus does not form haustoria but creates an intimate and intricate nutritional connection with the host cell wall (CW) and plasma membrane to acquire nutrients that alters the leaf structure (Bassi, Conti, and Barbieri 1984). Dissolution of the middle lamella, loosening of the CW structure, alterations in the plasma membrane, increase in the thickness of the mesophyll and loss of differentiation of palisade typically occur (Bassi, Conti, and Barbieri 1984; Giordani, Padula, and Radice 2013). Besides the mentioned microscopic studies on leaves with PLCD and the analysis of weather conditions that favour the infection (Rossi et al. 2006, 2007), only a limited number of biochemical studies have been conducted on PLCD. Raggi (1994, 1995) reported an increase in stomatal conductance and in transpiration in infected leaves, accompanied by a net decrease in photosynthesis and carbon fixation. Moscatello et al. (2017) documented a drastic diminish in photosynthesis and a decline in nonstructural carbohydrate content in infected trees. By challenging leaves of *P. persica* genotypes, susceptible or resistant to PLCD, with the fungus, we unravelled the early events of *P. persica-T. deformans* interaction (Svetaz et al. 2017). Besides the induction of reactive oxygen species, callose synthesis and defence compounds in both types of genotypes, differences in the timing and response were detected among genotypes. Transcript expression analysis indicated distinct hormonal responses, suggesting that defence mechanism observed in the resistant genotype may be mediated by salicylic acid. A metabolite profiling evidenced a biphasic response of the host after inoculation, indicating differences in early and later events that align with the development of the hyphae (Svetaz et al. 2017).

Peach apoplastic proteome analysis revealed the crucial role of the apoplast as a source of proteins involved in the perception and response to *T. deformans*. Common responses to pathogen in susceptible and resistant genotypes may be part of a basal defence machinery that includes pathogenesis-related proteins (PRs) acting on pathogen CW. Conversely, the induction of some PR5 isoforms, a PR12 and PR17 in the resistant genotype may constitute a strategy to overcome the fungus (Butassi, Novello, and Lara 2022). Additionally, in asymptomatic infected leaves, chloroplasts were denoted as a key compartment for peach defence responses (Goldy et al. 2017).

The objective of this study was to comprehensively investigate the biochemical and physiological imbalances in leaves exhibiting PLCD. Employing an integrated approach that includes large-scale techniques such as metabolomics, lipidomics, and proteomics, the metabolic processes occurring in leaves with PLCD were explored in symptomatic and asymptomatic leaf areas of leaves with different degrees of the disease. Symptomatic areas showed an altered chloroplastic functioning and composition, decreases in triacylglycerols double bond index, upregulation of phenylpropanoid and mevalonate pathways and increased asparagine. Curled areas exhibited a metabolic shift towards functioning as a sink tissue importing sugars and producing energy through fermentation and respiration and reductive power via the pentose phosphate route.

2 | Materials and Methods

2.1 | Plant Material

Leaves were collected from plants of *Prunus persica* L. advanced selection DOFI-84.364.089 grown at the EEA-INTA, San Pedro, Argentina (Bellini et al. 2002; Goldy et al. 2017). Fungicides were not applied to this orchard to allow the natural development of PLCD.

2.2 | Tissue Sampling and Processing

Collected leaves were classified according to the scale of susceptibility (Ritchie, 1981); where grade 0 (G0) corresponds to no visible symptoms; grade 2 (G2): chlorosis and curl area less than 1 cm; grade 7 (G7): 25%– 50% of area thickening and curving; and grade 8 (G8): 50%–75% of area thickening and curving. In

G2, G7 and G8 leaves areas exhibiting symptoms (C) were separated from those of normal appearance (N). Plant material was frozen in $N_{2(l)}$ and kept at −80°C.

2.3 | *T. deformans* Detection in Peach Leaves

The presence of fungus in peach leaves was tested by fungal DNA amplification using DNA extracted from leaves which contain both fungal and plant DNA followed by amplification of the *T. deformans* ITS1 region using PCR as described in Goldy et al. (2017). Results were expressed as percentage of positive (presence of 1132 bp amplification band) samples among tested samples of the same type. Fifty-eight asymptomatic leaves were tested. Between five and 10 samples from G2N, G2C, G7N, G7C and G8N and G8C were evaluated.

2.4 | Dry Matter

Representative samples were weighed to record the FW and reduced to dryness at 80°C until no further weight change had occurred (DW). Dry matter (%) was expressed as 100 × DW/FW.

2.5 | Pigment Analysis

Chlorophylls and carotenoids were spectrophotometrically quantified (Wintermans and De Mots 1965). Phenolic compounds were extracted and measured using the Folin reagent (Merck); and a phenol-calibration curve (Cantín, Moreno, and Gogorcena 2009).

2.6 | Protein Extraction

Samples were ground in $N_{2(l)}$ and total protein was extracted in 100 mM Tris-HCl, pH 8.0; 1 mM EDTA; 10 mM $MgCl_2$; 10 mM β-mercaptoethanol and 20% (v/v) glycerol. After centrifugation at 10 000 *g* for 15 min at 4°C, the supernatant was used for protein quantitation and diluted in 0.25 M Tris-HCl, pH 7.5; 2% (w/v) SDS; 0.5% (v/v) β-mercaptoethanol and 0.1% (v/v) bromophenol blue and boiled for 2 min for SDS-PAGE or precipitated with trichloroacetic acid (TCA) for proteomic analysis.

Protein concentration was determined as in Borsani et al. (2009).

2.7 | SDS-PAGE and Western Blot Analysis

SDS-PAGE was performed according to Laemmli (1970). Proteins were visualized with Coomassie blue or electroblotted onto a nitrocellulose membrane and incubated with 1:200 sera against *Amaranthus viridis* phospho*enol*pyruvate carboxylase (PEPC; Colombo, Andreo, and Chollet 1998); 1:10 000 sera against spinach RuBisCO large subunit (LSU) or 1:1000 antibodies against *Triticum aestivum* ADP-glucose pyrophosphorylase (AGP, Peralta et al. 2016). Bound antibodies were located by linking to alkaline phosphatase-conjugated goat anti-rabbit IgG diluted 1:1000 according to the manufacturer's instructions (Promega). Resolving gels were 10% (w/v) for RuBisCO and 8% (w/v) for PEPC and AGP immunoblotting.

Quantification of the intensity of the bands was conducted using Image J (https://imagej.nih.gov/ij/) software in at least three independent blots. In the case of PEPC, the amount of the upper band was quantified separately from the lower band.

2.8 | Proteomic Analysis Through High-Resolution Mass Spectrometry

Forty micrograms of proteins extracted from G0, G7N and G7C were precipitated with 1/5 volumes of 100% (w/v) TCA overnight at −20°C. The pellet was washed twice with cold acetone and proteins were finally resuspended in 50 μL 8 M urea and reduced with 10 mM DTT for 45 min at 56°C. After alkylation with 20 mM iodoacetamide for 40 min, proteins were precipitated with 1/5 100% (w/v) TCA overnight, washed with cold acetone, dried and delivered to the Proteomics Core Facility CEQUIBIEM, Buenos Aires, Argentina. Proteins were resuspended in 50 mM NH_4HCO_3, pH 8 and digested overnight with sequencing-grade modified trypsin (Promega). Zip-Tip C18 (Merck Millipore) columns were used for desalting. Resulted peptides were separated in a nano-HPLC (EASY-nLC 1000, ThermoScientific, Germany) coupled to a mass spectrometer with Orbitrap technology (Q-Exactive with High Collision Dissociation cell and Orbitrap analyzer, ThermoScientific, Germany). Peptides were ionized by electrospray. Proteome Discoverer 2.1 software (ThermoScientific, Germany) and the peach reference proteome set from Uniprot (*P. persica* (*Amygdalus persica*)-UP000006882-Uniprot) were used to identify peptides and proteins. Three biological replicates were used for each sampled analyzed.

The analysis of the differential proteomes was conducted using the Perseus 1.6.1.3 software platform (http://www.perseus-framework.org; Tyanova et al. 2016). Each comparison (G7N vs. G0 and G7C vs. G0) was independently analyzed. The normalized areas of total identified proteins were filtered so that only proteins that had at least two out of three biological replicates with valid values in each condition were taken into account in the statistical analysis. Afterwards, two-sample tests were conducted to compare proteomes of G7N versus G0 and G7C versus G0 by applying the standard *t*-test statistic with a permutation-based false discovery rate of 0.05. A q-value ≤ 0.05 and $0.5 < \text{fold change (FC)} < 1.5$ were used as significance threshold parameters (p-value < 0.05). Volcano plots showing q-values ($-\log_{10}$) depicted against $\log_2$ FC were used to assess differences between samples.

On the other hand, proteins that were not identified in any of the biological replicates of one condition but presented two to three valid values in the other were studied separately as follows. When a protein had valid values in G7N or G7C but not in G0, it was denoted with a (+) to indicate the presence of that protein in those samples and the absence in G0. Contrariwise, if a protein exhibited valid values only in G0 but neither in G7N nor in G7C, it was designated with a (−) to indicate the absence of that protein in G7N or G7C and the presence in G0.

Proteomic data was also subjected to an unsupervised clustering method (principal component analysis, PCA) using the R packages "Prcomp" and "factoextra."

Ontology annotations of significantly regulated proteins for biological process were analyzed to assess common localizations and functions by using MapMan (Schwacke et al. 2019).

Subcellular localization of selected proteins was analyzed using protein sequence and the following bioinformatic tools: Target P-2.0, Signal P-5.0 or 6.0 and DeepLoc-2.0 at DTU Health Tech (www.services.healthtech.dtu.dk).

2.9 | Polar Metabolite Measurements

Metabolite profiling was conducted by GC-MS according to Roessner-Tunali et al. (2003) and Monti et al. (2016) using an AS 2000 autosampler, a GC 8000 gas chromatograph, and a Voyager quadrupole mass spectrometer (Thermo Finnigan, Manchester, UK). A 30 m SPB-50 column with 0.25 mm inner diameter and 0.25 μm film thickness (Supelco, Bellefonte, CA, USA) was used for metabolite separation. One hundred milligrams of leaf FW was used for extraction. Ribitol was added as internal standard. Derivatization was conducted by using methoxyamine hydrochloride in pyridine and *N*-methyl-*N*-[trimethylsilyl]trifluoroacetamide. The Golm Metabolome Database was used as reference (Kopka et al. 2005). Five biological replicates were investigated. Data were normalized before analysis. Results are presented following Fernie et al. (2011) recommendation. Metabolite Reporting Guidelines (Checklist table) were those published in Svetaz et al. (2017).

Sorbitol was measured enzymatically using sorbitol dehydrogenase from sheep (Sigma, St Louis, MO, USA, Borsani et al. 2009).

For starch quantification, 50 mg of tissue was incubated with 600 μL of methanol for 15 min at 70°C, then 500 μL of cold H_2O was added, vortexed and centrifuged at 14 000 *g* for 15 min. The pellet was incubated with 200 μL of 0.2 M NaOH for 45 min at 95°C, brought to pH 4.5–5 with 5 M acetic acid and centrifuged during 10 min at 14 000 *g*. Samples were incubated overnight at 25°C with α-amylase (2.5 U) and amyloglucosidase (3.5 U). After centrifugation for 15 min at 14 000 *g*, the supernatants were used for glucose quantification using the glucose oxidase method (Wiener lab) and the manufacturer's instructions.

2.10 | Lipid Extraction and LC–MS Analysis

Lipids were extracted from 100 mg of tissue using a methanol: methyl tert-butyl ether: water (1:3:1) mixture according to Bustamante et al. (2018).

An Acquity Ultra Performance Liquid Chromatography (UPLC) system (Waters, Milford, MA) equipped with a C8 reversed phase column (100 mm × 2.1 mm × 1.7 μm particles waters) was used for lipid separation, coupled with an Exactive mass spectrometer (Thermo-Fisher, Carlsbad, CA). Injection, running conditions, mass spectra acquisition, chromatograms analysis and peak annotations were performed as exactly described previously (Bustamante et al. 2018). REFINER MS 5.3 (GeneData) was used for chromatogram analysis.

Levels of individual lipid species were normalized to both the total ion count of each sample and across the day of measurement to decrease batch effect. Biological quintuplicates were analyzed.

The double bond index was calculated as in Bustamante et al. (2018).

2.11 | Thiobarbituric Acid Reactive Substances (TBARS)

Malondialdehyde (MDA) was quantified as in Righini et al. (2019). Controls were performed to evaluate for and subsequently discount any interference from anthocyanins.

2.12 | Data and Statistical analysis

The GC-MS and UPLC-MS data were subjected to PCA and Pearson correlation analysis (p-value < 0.05) using the R packages "Prcomp" and "factoextra." Heat maps were created with MultiExperiment Viewer (MeV v4.9.0, https://webmev.tm4.org/, Saeed et al. 2003) software.

All data presented were expressed as mean ± SD of at least five independent replicates.

Metabolome and lipidome data were analyzed using the "Agricolae" Package from Rstudio. Kruskal–Wallis and Bonferroni tests were used.

Other measurements were analyzed using one-Way ANOVA. Minimum significance differences were calculated by the Bonferroni, Holm–Sidak ($\alpha = 0.05$) using the Sigma Stat Package.

3 | Results

3.1 | Morphological and Biochemical Features of *T. deformans* Infected Leaves

Fully expanded leaves, from *P. persica* trees naturally infected with *T. deformans*, exhibiting leaf malformations were studied (Figure 1). Infected zones are thickened and wrinkled and show increased anthocyanin pigmentation. As the extent of distorted region increases, the leaves get curly (Figure 1B, G8). To study the biochemical changes in symptomatic areas, leaves were classified according to the grade of PLCD (Figure 1B) and dissected as shown in Figure 1C. In addition, the presence/absence of the fungus was tested by PCR in each type of tissue. The fungal DNA was not detected by molecular procedures in 58 asymptomatic leaves classified as G0. With respect to asymptomatic regions, fungal DNA was not detected in G2N or G7N leaves, while a 16.6% of the samples were positive in G8N

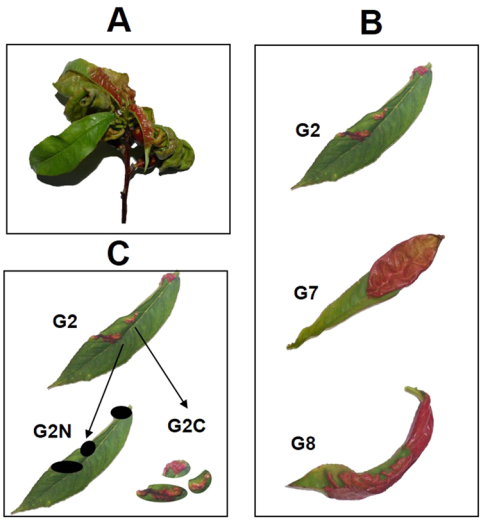

FIGURE 1 | Morphological features of *Prunus persica* leaves showing *Peach leaf curl disease*. (A) Image illustrating a typical infected branch. (B) Leaves with different grades of the disease are shown: G2, grade 2, less than 1 cm of the leaf exhibits symptoms; G7, grade 7, a 50% of the leaf area presents leaf curl and thickening, and G8, grade 8, up to the 75% of the leaf shows typical symptoms of the disease. (C) Representation of leaf processing. First, leaves were classified as no visible signs of leaf curl (G0) or according to the extent of the disease (G2, G7 or G8). Then, using G2, G7 and G8 leaves, the areas exhibiting curl and thickening (C) were separated from the areas with no symptoms (N).

leaves. In symptomatic areas, the proportion of positive samples for the fungal DNA detection by the technique used increased with the degree of the disease (20%, 30%, and 50% in G2C, G7C and G8C, respectively, Supporting Information S1: Figure S1).

Regardless the degree of the disease, chlorophyll and carotenoids show a great decline in sections exhibiting PLCD (C) in comparison with asymptomatic areas (N) and healthy leaves (G0) (Figure 2). Protein content in symptomatic areas (G2C, G7C and G8C) does not vary with respect to healthy leaves (G0); however, the protein content of asymptomatic zones is higher than in G0. The dry matter tends to decrease with the degree of the disease, with G8C being 54% lesser than that of G0. Total soluble phenolic content was not affected in G2 and G7 leaves with respect to G0. Anthocyanins were increased in G2C, G7C and G8C with respect to G0. Chlorophylls and carotenoids greatly decreased in symptomatic areas (Figure 2).

3.2 | Metabolomic Analysis of *P. persica* Leaves

Metabolomic profiling conducted by GC-MS allowed the identification of 67 different metabolites in *P. persica* leaves that were classified in amino acids (19 metabolites), organic acids (15), sugars (16), alcohol sugars (five), fatty acids (two) and miscellaneous (10) (Figure 3A). The levels of each metabolite are shown in Table S1 and the plots showing the statistical analysis are presented in Supporting Information S1: Figure S2.

Two principal components (PCs) explain the 58.7% of the global variance of metabolite profiles (31.6% and 27.1% for PC1 and PC2, respectively) and PC3 represents 9.5% of the global variance (88.5%). Irrespective of the extent of PLCD, samples from symptomatic areas group together while asymptomatic areas cluster in another group (Figure 3B). Interestingly, asymptomatic leaves (G0) group together with asymptomatic areas of affected leaves in PC1 versus PC2 plots (G2N, G7N and G8N). The variable contribution to each PC is listed in Table S2 and main contributors are shown in Figure 3B.

Ala is the metabolite that exhibits the highest number of positive correlations (41), correlating with all amino acids except for Asn and Asp, and most sugars, organic acids and miscellaneous compounds (Supporting Information S1: Figure S3, Table S3). Thus, a common pattern observed is that of Ala, whose relative level significantly decreases in symptomatic areas (G2C, G7C and G8C) with respect to either healthy leaves (G0) or asymptomatic areas of leaves with PLCD (G2N, G7N and G8N). Instead, mannose was the metabolite that exhibits the highest number of negative correlations (27), followed by Asn and Xyl with 14 negative correlations. Mannose, Asn and Xyl are metabolites that exhibit increases in symptomatic areas with respect to G0. Asn tended to increase with the progression of PLCD in both asymptomatic and symptomatic areas, with maximum increase in G8C (34.4-fold with respect to G0).

To complete the biochemical profile, starch content significantly decreased in areas exhibiting signs of PLCD with respect to asymptomatic areas and with respect to healthy leaves. Moreover, as the degree of PLCD increased, starch tended to decrease in asymptomatic areas with respect to G0. Sorbitol content was also decreased in symptomatic areas of leaves with a high degree of PLCD (G7C and G8C) with respect to G0, G2N, G7N and G78N (Figure 3C).

3.3 | Lipidomic Analysis of *P. persica* Leaves

Lipid profiling was conducted for the first time in leaves (G0, G7 and G8) of *P. persica*. UPLC-MS allowed the identification of 132 distinct lipids representing 10 classes and subclasses: 22 phosphatidylcholines (PCs), 15 phosphatidylethanolamines (PEs), four phosphatidylglycerols (PGs), four phosphatidylinositols (PIs), seven diacylglycerols (DAGs), 51 (TAGs), five sulfoquinovosyl diacylglycerols (SQDGs), 12 monogalactosyl diacylglycerols (MGDGs) and 12 digalactosyl diacylglycerols (DGDGs) (Figure 4A, Table S4). TAGs with acyl chains containing 48; 50; 52, 54; 56; 58 and 60 carbons were identified. Up to nine unsaturations were detected in TAGs with 54 and 56 carbons in their acyl tails.

PCA was used to assess the overall biological differences in the lipid signals among samples (Figure 4B). The first three PCs explained 79.5% of the variance in the relative intensities of the lipids. As in the case of metabolomics, lipidomic analysis grouped symptomatic areas (G7C and G8C), separately from asymptomatic areas (G7N and G8N) of leaves. Species contributing to each component are listed in Table S5 and shown in Figure 4B.

Diacylglycerolipids, such as MGDGs, DGDGs and SQDGs negatively correlated with TAGs. In addition, MGDGs and DGDGs negatively correlated with most of phospholipids and positivity

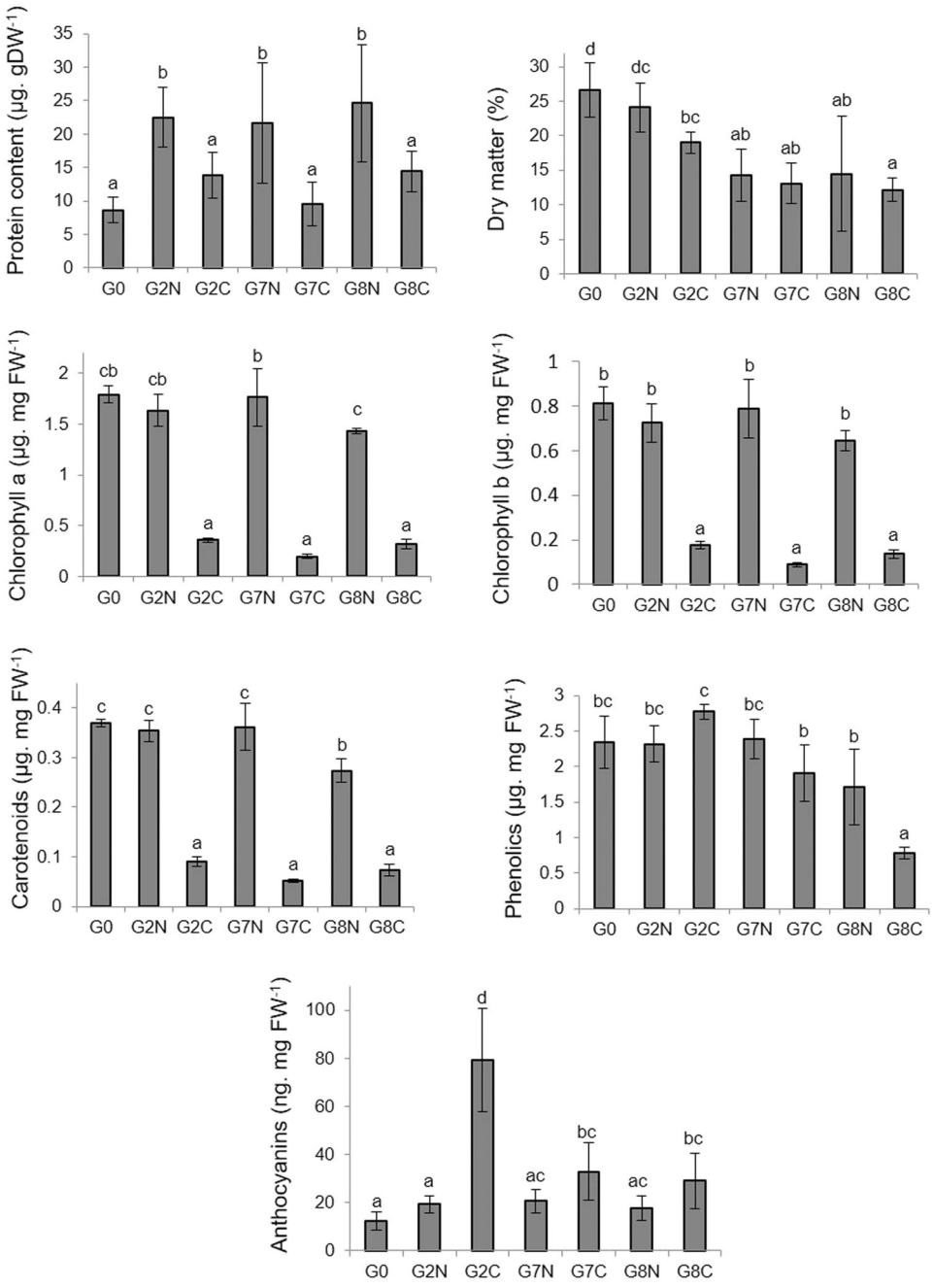

FIGURE 2 | Pigment, proteins and percentage of dry matter quantification. The levels of proteins, chlorophylls, carotenoids, total phenolics and anthocyanins were measured and expressed in a fresh weight (FW) basis. Values represent the mean of at least five independent determinations ± the SD. The ratio between dry (DW) and fresh weights (FW) × 100 is the dry matter content (%), $n = 15$. Bars with at least one same letter are not statistically different (p-value < 0.05).

correlated with SQDGs. Some DAGs positively correlated with MGDGs and DGDGs, and MGDGs positively correlated with DGDGs. TAGs positively correlated among each other (Supporting Information S1: Figure S5, Table S6).

In general, PCs (16 out of 22), PIs (four out of four PIs species), PEs (12 out 15 PEs species), PGs (two out of four PG species) and MGDGs (seven out of 12 species) tended to increase in symptomatic areas from infected leaves with respect to G0. Conversely, DGDGs 32:0, 34:4, 36:4, 36:5(2) and 38:6 decreased in G7C and/or G8C with respect to G0 reaching values up to a 40% of G0 in the case of DGDG 32:0. Notably, SQDG 36:6 diminishes an 85% and a 70% in G7C and G8C with respect to G0, respectively. With the exception of MGDG 34:6, which decreased, statistically significant changes in MGDGs in symptomatic areas with respect to G0 were related to increases in these species (Figure 4A and Supporting Information S1: Figure S4, Table S4).

In the case of storage lipids, the most prominent changes in TAGs were found in symptomatic areas of diseased leaves with respect to G0, with TAGs with low number of unsaturations (48:0, 48:1, 48:2, 48:3, 50:0, 50:1, 50:2, 52:0, 52:1, 52:2, 52:3, 54:0, 54:1, 54:3, 54:4, 56:1, 58:1, 60:2, 60:3) being increased in G7C

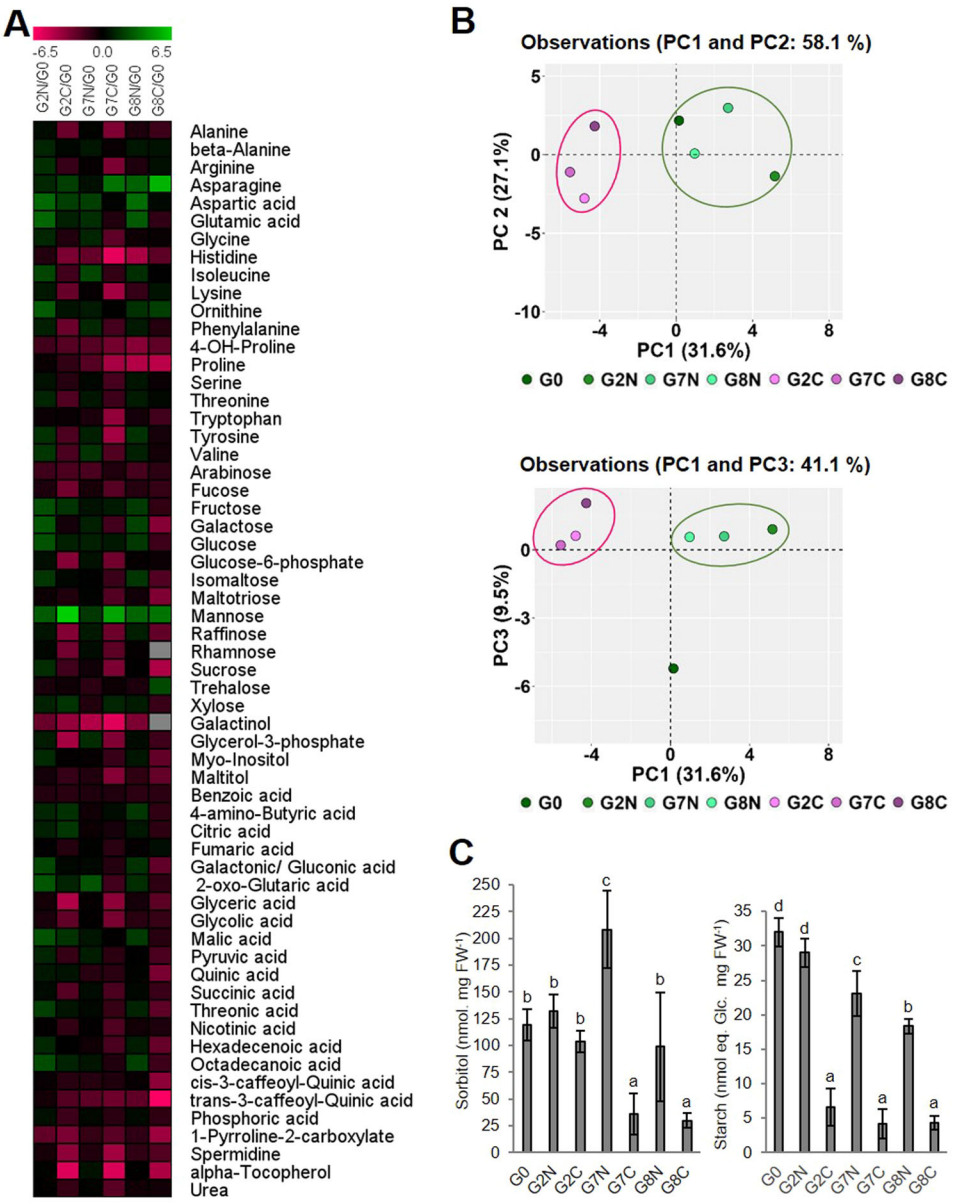

FIGURE 3 | Metabolite profiling in curled and healthy leaves of *P. persica*. (A) Heat map representing metabolite profiling performed by GC-MS. The heat map displays the relative level of each normalized metabolite to its amount found in G0 leaves (healthy leaves) and expressed as log2. The colour scale is shown at the top of the figure and it is proportional to the content of each metabolite. Grey colour indicates that the metabolite was not detected, therefore there is not assigned value. At least five biological independent determinations were analyzed for each sample. Relative values for each metabolite peak area ± SD are displayed in Table S1 and plotted with their corresponding statically analysis in Supporting Information S1: Figure S2. (B) Principal component analysis (PCA) of metabolite composition by GC-MS. Between parentheses, the variance explained by each component (%) is shown. (C) Sorbitol and starch contents enzymatically determined. Starch amount is expressed as nmols of glucose released per milligram of fresh weight. Bars with at least one same letter are not significant statically different. [Color figure can be viewed at wileyonlinelibrary.com]

and/or G8C with respect to G0. Most notably, TAG 58:1 exhibited a rise of 97-times, and TAG 48:1 and 50:1 an increase of 63-fold in G8C with respect to G0. Conversely, highly unsaturated TAGs (50:4(1), 50:5, 52:6, 52:7, 54:9, 56:5, 56:6, 56:9, 58:4, 58:5, 58:6, 60:5) decreased in symptomatic tissue with respect to G0, with most remarkably decreases in 52:7 and 56:9 being reduced to an amount of 0.08- and 0.15-times in G8C with respect to G0 (Figures 4A and S4, Table S4).

By contrast, only a few TAGs increased in asymptomatic areas of infected leaves (G7N, and G8N) with respect to G0 (48:1; 50:0; 52:0, 54:0 and 60:6). Instead, TAGs 50:5, 52:4, 52:5, 54:2, 54:5, 54:6, 54:7, 56:2; 56:3, 56:4, 56:5, 56:6, 56:7, 58:5, 58:3, 58:4, 58:5, 58:6, 60:3, 60:4, 60:5 decreased in G7N and/or G8N with respect to G0 (Figure 4A and Supporting Information S1: Figure S4, Table S4). A total mass spectral signal was computed for TAGs (Figure 5A), while TAGs were accumulated in symptomatic areas with respect to healthy leaves, the total level of TAGs decreased in asymptomatic areas with respect to G0.

The double bond index (DBI) computed for each lipid species was decreased in TAGs from PLCD leaves with respect to G0 (Table S7).

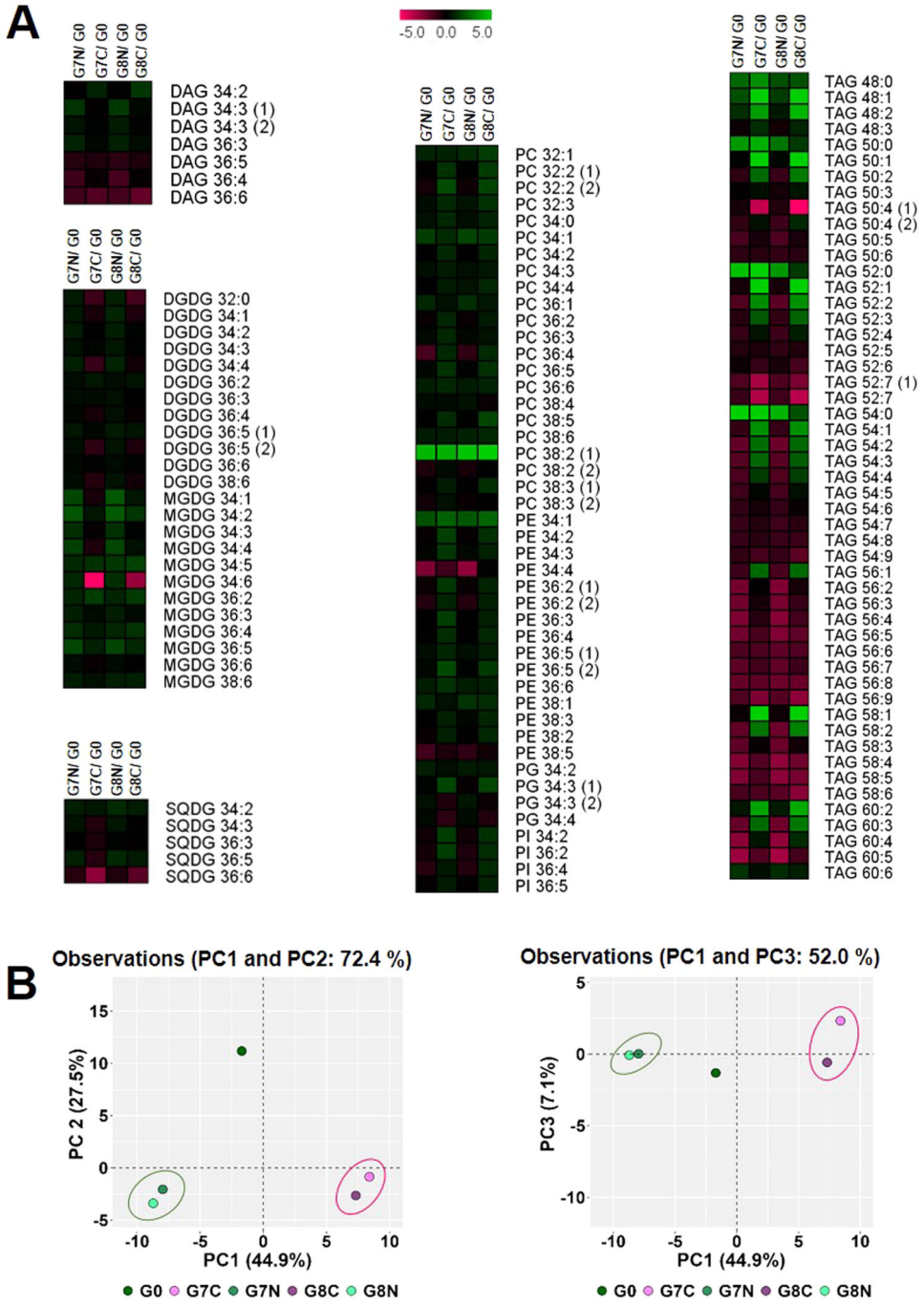

FIGURE 4 | Lipid profiling performed by UPLC-MS. (A) Heat map. The heat map displays the relative level of each normalized lipid to its amount found in G0 leaves (no visible symptoms of disease) and expressed as log2. The colour scale is shown at the top of the figure and it is proportional to the content of each metabolite. At least five biological independent determinations were analyzed for each sample. Relative values for each metabolite peak area ± SD are displayed in Table S4 and plotted with their corresponding statistical analysis in Supporting Information S1: Figure S4. Lipid species are annotated based on a C *x*:*y* nomenclature where *x* represents the total carbon number and *y* is the total number of bound. The numbers between parentheses indicate the presence of different isomers of the same lipid which differ in position of the double bond. For example DGDG36:5 (1) and DGDG36:5 (2). (B) Principal component analysis (PCA) of lipid profiling. Between parentheses, the variance explained by each component (%) is shown. [Color figure can be viewed at wileyonlinelibrary.com]

While DBI decreased in both symptomatic and asymptomatic areas with respect to G0; the greatest diminishes were observed in G7C and G8C with respect to G0. Therefore, DBI was calculated for each subtype of TAG, based on the total carbon number (Figure 5B). In each type of TAG, the DBI decreased in G7C and G8C with respect to G0. DBI also tended to decrease in G7N and G8N in TAGs with 48 and 50 carbons. These results reveal a reconfiguration of acyl-chains in TAGs from an unsaturated to a more saturated state in leaves showing PLCD.

A MDA assay was conducted to explore lipid peroxidation. MDA increased by 49% and 38% in G7C and G8C with respect

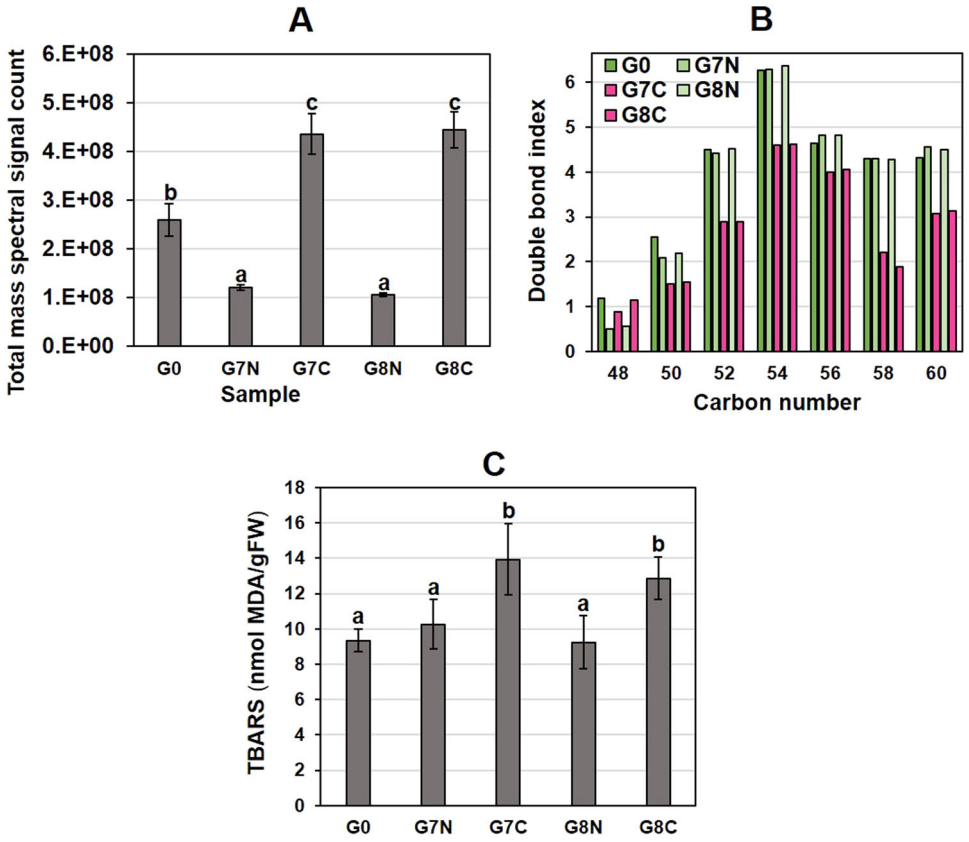

FIGURE 5 | (A) TAGs accumulation. The total mass spectral signal in UPLC-MS profiling for the different TAGs is computed. (B) Double bond index of TAGs. TAGs were grouped based on the total carbon number. The DBI was calculated based on the results of lipid profiling generated by UPLC-MS. (C) Lipid peroxidation. Thiobarbituric acid reactive substances (TBARS) were measured as indicative of lipid peroxidation in healthy and LPCD-leaves. Values represent the mean of at least five independent determinations ± the SD. Bars with at least one same letter are not statistically different (p-value < 0.05) according to Kruskal–Wallis analysis. [Color figure can be viewed at wileyonlinelibrary.com]

to G0, respectively. While no differences in the TBARS were observed between G0, G7N and G8N (Figure 5C).

3.4 | Proteomic Analysis of *P. persica* Leaves

Metabolomics and lipidomics revealed G2, G7 and G8 leaves exhibit a similar behaviour; thus, G7 leaves were chosen for proteomic comparisons. A total of 1725 unique *P. persica* proteins were identified in G0, G7N and G7C which covered a 7.7–411.5 kDa range and a 3.87–12.2 pI. Information regarding proteins, number of peptides, sequence coverage and label-free quantification values are presented in Table S8A. In addition, only 58 unique proteins corresponded to *T. deformans*, which covered a 14.4–118 kDa range and a 4.75–16.64 pI. Therefore, proteome analysis was conducted only for *P. persica* proteins (Table S8B). The PCA of protein abundance reveals that proteomes of G0 and G7N are closer than that of G7C, as observed for the metabolome analysis (Figure 6A). It is worth to mention, that proteomes are compared in a protein by protein manner. In this way, although the protein composition is similar in both tissues, the protein content per gram fresh weight (FW) is higher at G7N with respect to G0 (Figure 2).

To identify differences in protein expression in G0 against G7N or G7C statistical analysis were conducted and plotted in volcano plots (Supporting Information S1: Figure S6). Differentially abundant proteins (DAPs) varying in a factor greater or smaller than 1.5; or with the presence of the signal in only one of the two samples compared were considered for further analysis (Table S10). Among detected proteins, 573 varied in at least one sample of the comparisons. Proteome analysis of G7N versus G0 identified only 39 DAPs, while G7C versus G0 rendered 560 DAPs. In G7N versus G0, 22 proteins were induced and 17 proteins were decreased. In G7C versus G0, 363 proteins were upregulated and 197 proteins were downregulated (Figure 6B).

An overview of the biological functions of DAPs reveals that in the comparison of G7N with G0 there was a significant enrichment in miscellaneous and uncharacterized proteins (28%), followed by stress response (10%), secondary metabolism (10%), protein metabolism and translocation (10%) and CW organization (8%). The most represented categories in the comparison G7C versus G0 were protein metabolism and translocation (26%), carbohydrate metabolism and cellular respiration (12%), miscellaneous and uncharacterized (11%), photosynthesis (10%), stress response (8%), amino acid metabolism (5%) and secondary metabolism (5%) (Figure 6C).

Dissected GO analysis terms are shown for the enriched categories in each comparison (Figure 7). Comparing the proteome of G7C versus G0, within protein metabolism and translocation, a 20% of DAPs corresponded to downregulated proteins

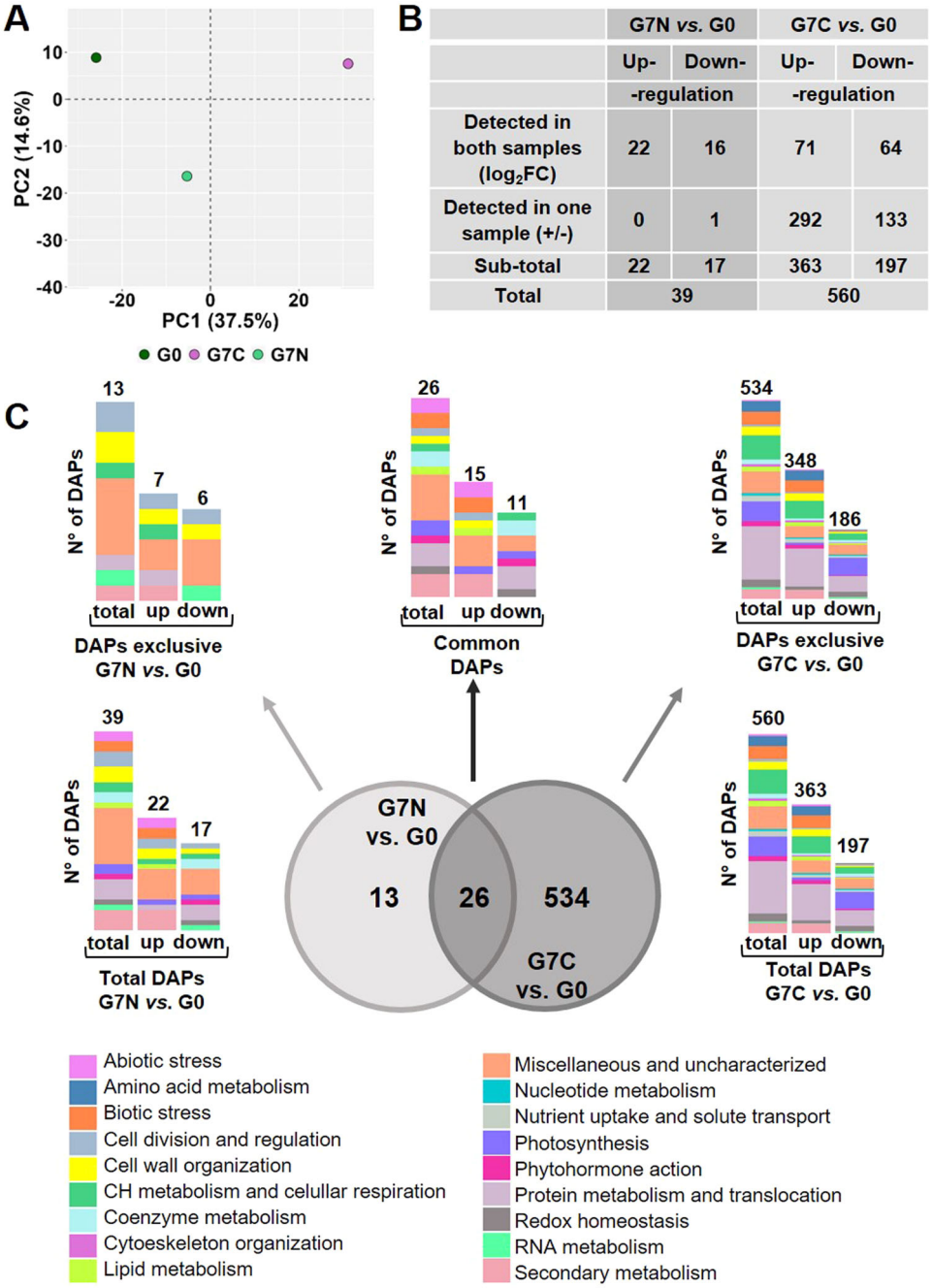

	G7N *vs.* G0		G7C *vs.* G0	
	Up-regulation	Down-regulation	Up-regulation	Down-regulation
Detected in both samples (log_2FC)	22	16	71	64
Detected in one sample (+/-)	0	1	292	133
Sub-total	22	17	363	197
Total	39		560	

FIGURE 6 | Proteome analysis of PLCD leaves. (A) Principal component analysis (PCA) of protein profiling. Between parentheses, the variance explained by each component (%) is shown. (B) Summary of differentially accumulated proteins (DAPs). Up- and downregulated proteins were computed using Perseus software. p-value < 0.05, 0.05% FDR and q-value < 0.05, DAPs were filtered based on 0.5 < FC < 1.5. Proteins present in one of the samples of the comparisons but absent in the other sample were also computed as (+) and (−) as depicted in Table S10. (C) Functional classification according to MapMan ontology. Proteins are grouped based on the total number of proteins in the comparison (total), up- or downregulated proteins. The Venn diagram shows the number of DAPs in the comparisons G7N versus G0 and G7C versus G0. [Color figure can be viewed at wileyonlinelibrary.com]

involved in cytosolic protein biosynthesis constituting ribosomes, having aminoacyl-tRNA synthetase activities or acting as factors in the translation, and a 32% corresponded to increase in proteins involved in protein degradation through the ubiquitin-proteasome system or other proteases. Chloroplastic protein metabolism and translocation was also modified, with the 13% of these DAPs belonging to organelle machinery including ribosomal LSU, SSU, initiation, elongation and ribosomal recycling factors, and four involved in protein translocation being downregulated in G7C versus G0 (Table S10).

In symptomatic areas (G7C) there was a pronounced downregulation in proteins involved in photosynthesis with respect to G0. Decreased proteins include different steps of photophosphorylation like those involved in photosystem II (PSII, M5VQZ6, M5VXT9,

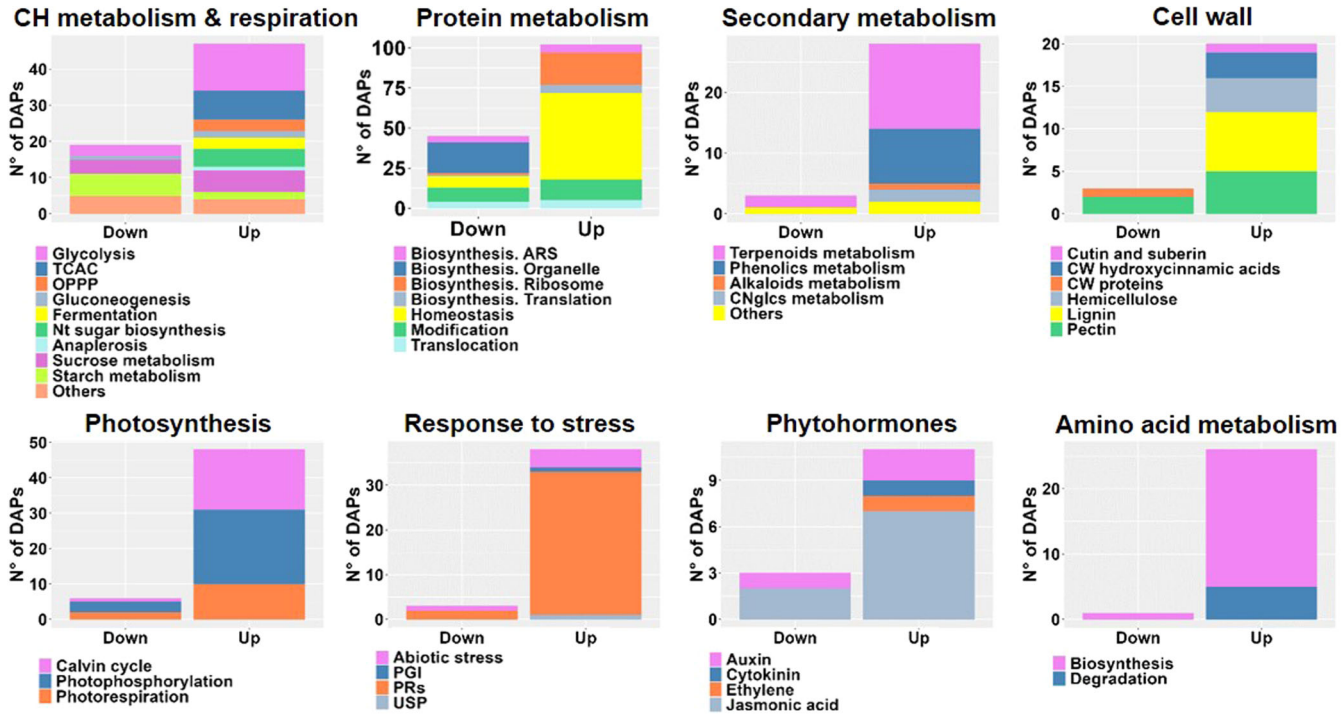

FIGURE 7 | Visualization of proteomic variations in symptomatic areas (G7C) with respect to healthy leaves (G0). Distribution of DAPs in the most represented functional categories by MapMan analysis. Up- and downregulated proteins are shown separately. ARS, Aminoacyl-tRNA synthetase; BCAA, branched-chain amino acid; Nt, nucleotide; OPPP, oxidative pentose phosphate pathway; PGI, pathogen polygalacturonase inhibitor; TCAC, tricarboxylic acid cycle; USP, universal stress protein. [Color figure can be viewed at wileyonlinelibrary.com]

M5WUI4, M5WUX4, M5WHI4, M5WTF3, M5WIR6, M5X0Q9, M5WTM9, M5XD80, M5X424, M5W031, M5W4K8, M5VWI3, M5W6E3), plastocyanin (M5XH36), ferredoxin-NADP reductase (M5W912), FNR interacting protein (M5VMA7) and ATP synthase complex (E3W0K0, E3W0J9); the Calvin Cycle including RuBisCO-LSU (E3W0K1), -SSU (M5XB14), -activase (M5XKY5, M5WHT2, M5VY27 and M5X8A8) and enzymes participating in carbon reduction and ribulose-1,5-P_2 regeneration (M5WBF3, M5WY11, M5WN82, M5WF88, M5WZ53, M5VSP4, M5VP21, M5VYL1, M5X0I6, M5XJR4, M5VZJ1); and photorespiration (M5W0C3, M5X0S5, M5XR34, M5WVV0, M5Y8B9, M5WH65, M5WVV1, M5VXS4, M5W8G7, M5VW13). Conversely, NAD(P)H dehydrogenases (M5WHH6, M5WV99) involved in chlororespiration, and serine hydroxymethyltransferases (M5XYL0 and M5XDY2) and PEPC (M5WNQ0) were upregulated in symptomatic areas (Table S10, Figure 7).

Changes in enzymes involved in carbohydrate metabolism and cellular respiration were observed in G7C versus G0 (Table S10, Figure 7). Starch biosynthetic enzymes were diminished while a plastidial alpha-amylase was induced. Regarding sucrose metabolism, increases in degradative sucrose synthases (M5W5U6, M5VWQ6) and invertase (M5XEX0), and in biosynthetic sucrose-P-phosphatase (M5W745) were recorded. Additionally, sorbitol-6-phosphate dehydrogenase (A5JUQ9) catalyzing in sorbitol biosynthesis was downregulated. Regarding glucose catabolism, upregulation of enzymes related to cytosolic (M5WS41, M5XJJ3, M5VRJ4, M5VPR4, M5WQC0, M5WH94, M5W2H9, M5WD83, M5XQ59, M5W5K0, M5VW31) and plastidial glycolysis (M5W7I6, M5WQ49), pyruvate fermentation (alcohol dehydrogenases, ADHs; M5VM41, M5VW29 and M5VJ94), pyruvate oxidation (pyruvate dehydrogenases; M5XYZ4 and M5XCC8) and in the tricarboxylic acid cycle (TCAC, M5WXP5, M5WZR5, M5VSW8, M5XA02, M5X4U1, M5VJR8, M5W1V2, M5VLX7) were found. Induction of enzymes of the oxidative pentose phosphate pathway (OPPP, glucose-6-phosphate dehydrogenase, M5XB81; 6-phosphogluconate dehydrogenase, M5WX92; Transaldolase, M5XW60) were observed.

Immunoblots confirm the patterns of decrease in RubisCO and increase of PEPC in G7C with respect to G0, and reveals a similar trend of variations in G2C and G8C as in G7C (Supporting Information S1: Figure S7). Downregulation of AGP was observed in G8C with respect to G0 and with respect to asymptomatic areas (G2N, G7N and G8N).

The 93% of DAPs in response to external stimulus group were increased in G7C with respect to G0 (Figure 7). Most of them are pathogen responsive proteins, many of which are classified as PRs. The following proteins were increased in G7C with respect to G0; PR1 (M5VJ82, M5W0E5), glucan endo-1,3-beta-glucosidases (PR2; M5WAH4, M5VQU4, M5X0X3, M5VM18), chitinases or chitin binding protein (PR3,-4,-8,-11; M5VMR9, M5Y0J0, M5X1D0, M5X1P7, M5VQE4, M5WI79, M5X3J0, M5Y9E2, M5W1Q5), thaumatin-like proteins (TLPs, PR5; M5WTQ8, M5WV03, M5WA70, M5WR50, M5WT96), proteinase inhibitor (PR6; M5XDT7), peroxidases (PR9; M5W061, M5W6X8, M5W030) and Bet_v_1 domain-containing proteins or major latex proteins (PR10; M5XFH8, M5XL43, M5XM39, Q9AXU0, M5XFD0, M5XTD1, Q2I6V8, M5XTC6). The only DAP classified as PR16 (M5WAE7) was downregulated in G7C versus G0 (Table S10).

Secondary metabolism was significantly upregulated in G7C with respect to healthy leaves (Table S10). Regarding terpenoid metabolism (Figure 8A), enzymes involved in the cytosolic

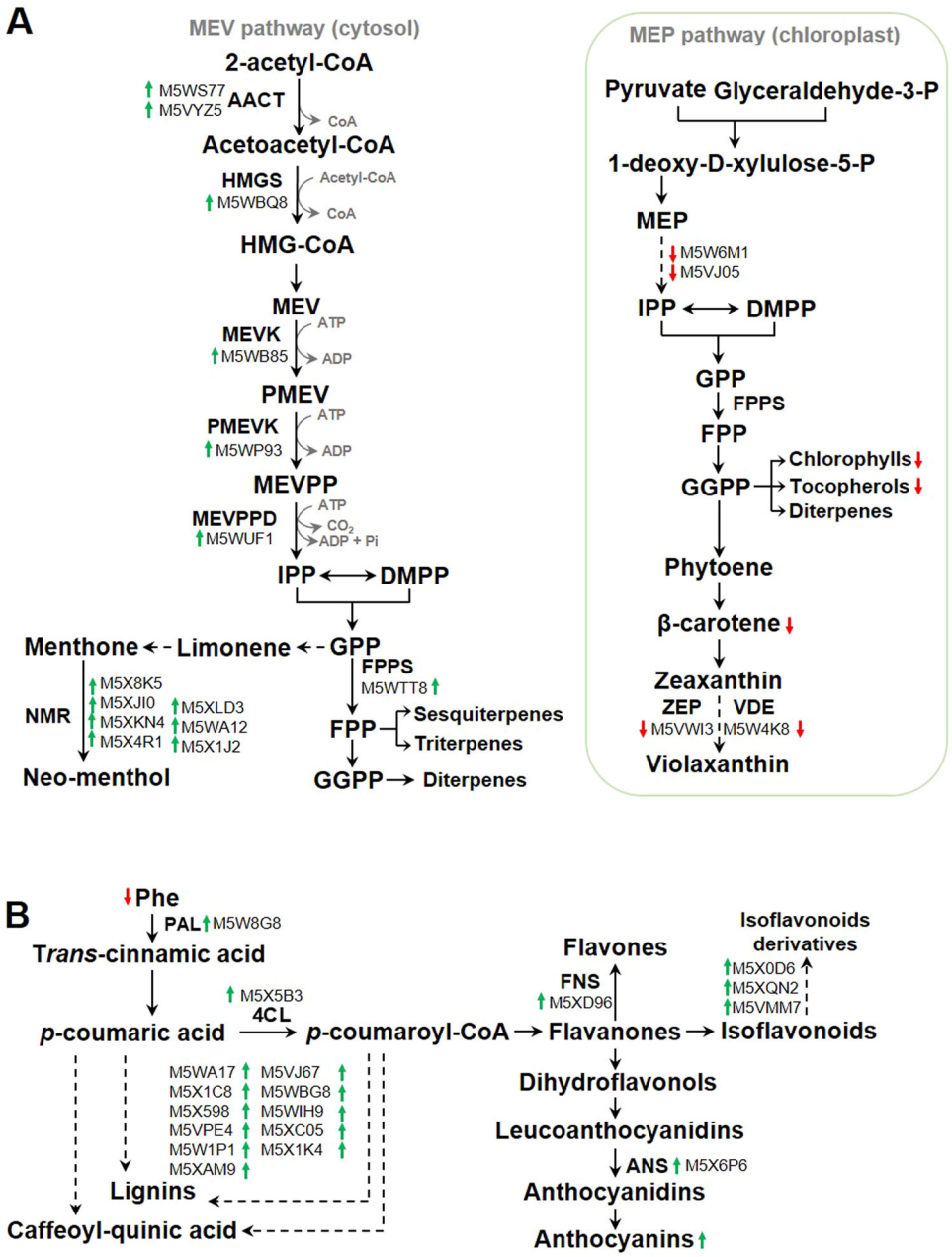

FIGURE 8 | (A) Schematic of the terpenoid pathways deriving from the mevalonate (MEV) and the methylerythritol phosphate (MEP) routs. Groups of terpenoids discussed in the manuscript are presented. AACT, acetoacetyl-CoA thiolase; DMPP, dimethylallyl pyrophosphate; FPP, farnesyl diphosphate, FPPS, FPP diphosphate synthase; GGPP, geranylgeranyl diphosphate; HMG-CoA, 3-hydroxy-3-methylgluratyl-CoA; HMGS, hydroxymethylglutaryl-CoA synthase; IPP, isopentenyl diphosphate; MEVK, MEV kinase; MEVPP, mevalonate diphosphate; MEVPPD, MEVPP decarboxylase; NMR, neomenthol dehydrogenase; PMEV, 5-phosphomevalonate, PMEVK, PMEV kinase; PMEV, 5-phosphomevalonate. (B) Simplified scheme of phenylpropanoid pathway showing DPAs in leaves with PLCD. 4CL, p-coumarate:CoA ligase; ANS, anthocyanidin reductase; FNS, Flavone synthase; PAL, phenyalanine ammonia-lyase. Reactions with a continuous arrow indicate one enzymatic step while dotted arrows represent more than one step. Protein Acc. N° of DAPs listed in Table S10 are indicated. Green ↑ represents a positive FC and red ↓ indicates a negative FC. [Color figure can be viewed at wileyonlinelibrary.com]

pathway of isopentenyl diphosphate (IPP) biosynthesis through the mevalonate pathway (M5WS77, M5VYZ5, M5WBQ8, M5WB85, M5WP93, M5WUF1) were upregulated in G7C with respect to G0, with M5WUF1 being the most upregulated within all DAPs detected ($\log_2$FC = 6.1, Table S10). A farnesyl diphosphate synthase (FPPS, M5WTT8) and seven accessions assigned as putative neomenthol dehydrogenases (NMRs) were also increased in G7C with respect to G0. Bioinformatic analysis predicted the cytosol as the most probable site for these enzymes (Table S11). Conversely, the plastidic methylerythritol phosphate (MEP) pathway that conducts to carotenoid, chlorophyll, tocopherol and xanthophylls synthesis was downregulated in symptomatic tissue with respect to G0.

Pathways related to phenylpropanoids, phenolics and flavonoids biosynthesis showed induced DAPs in G7C with respect

to G0 (Figure 8B). Enzymes involved in alkaloids (M5WGA1), cyanogenic (M5XBT1 and M5X090, Figure 9) compounds and putrescine (M5WUH8) biosynthesis were also up regulated.

Regarding phytohormones, it is of great relevance the upregulation of a tryptophan aminotransferase (M5VM03) involved in auxin biosynthesis through the indole-3-pyruvic acid pathway in G7C with respect to G0. In addition, two plastidic allene-oxide cyclases (AOCs, M5XB05 and M5XG39), three 13-lipoxygenases (LOXs, M5W6C3, M5X5W8 and M5WJG6) and two 12-oxophytodienoate reductases (M5XZ67 and M5VW19) involved in jasmonic acid biosynthesis were increased in G7C with respect to G0. Additionally, 1-aminocyclopropane 1-carboxylic acid oxidase (Q43618) involved in ethylene synthesis was also upregulated in G7C (Table S10). By contrast, no differential accumulation of enzymes related to auxin, ethylene and JA biosynthesis or degradation was found in the G7N versus G0 comparison. Finally, it is worth mentioning that besides M5X9V7 being classified as a cytokinin-conjugating enzyme, it encodes a quercetin glucosyltransferase.

With respect to CW organization, DAPs related to hemicellulose and pectin biosynthesis (1,4- β-glucan synthase, M5WL18 and M5XM62), degradation and modification (xyloglucan endotransglucosylase/hydrolase, M5XG58; xylan O-acetyltransferase, M5WGX3; β-galactosidase, M5XQ35; α-L-arabinofuranosidase, M5XKI2 and M5WE01, and pectate lyase, M5XN55) were upregulated and only one β-galactosidase (M5XF18) was downregulated. All the DAPs identified as enzymes involved in lignin biosynthesis were induced in G7C with respect to G0 such as cinnamoyl-CoA reductases (M5WA17 and M5X1C8) and dehydrogenases (M5WBG8, M5WIH9, M5XC05 and M5VJ67), caffeic acid O-methyltransferase (M5X1K4) and hydroxycinnamaldehyde dehydrogenases (M5XAM9, M5W1P1 and M5VPE4, Table S10).

4 | Discussion

To gain a more comprehensive understanding of the metabolic changes occurring in *P. persica* trees with PLCD, sick leaves were dissected separating curled tissue showing leaf hyperplasia and hypertrophy from asymptomatic tissue and both tissues were compared to healthy leaves. The fungus DNA was not detected by PCR in G0, G2N, and G7N samples, and it was detected in 16.6% of G8N leaves, where no leaf morphological changes were visible. In the case of symptomatic areas, the frequency of DNA fungal detection was also low, and the fungus was not detected in 80% of G2C, 70% of G7C, and 50% of G8C samples (Supporting Information S1: Figure S1). The high percentage of negative samples for the fungal DNA detection that show phenotypic alterations, as well as samples in which the fungus is detected but look healthy, suggests that changes in leaf-phenotype are not in direct relationship with the amount of fungus present; and thus, it indicates that morphological leaf alterations mostly depend on the leaf response. Alternatively, it is possible that the fungus is not distributed along the whole leaf area, as shown by Giordani, Padula and Radice (2013), who followed the progress of the disease through microscopy studies over the spring and found that *T. deformans* is distributed below the cuticle of the adaxial epidermis and in the palisade parenchyma in infected leaves. Moreover, maximum *T. deformans* observation occurs at very advanced times when symptoms exhibited maximum intensity (Grade 9 of Ritchie & Werner scale) and asci protrude the adaxial epidermis. In summary, considering the results presented here regarding fungal DNA detection (Supporting Information S1: Figure S1), the previous results that indicate that the amount of plant cells is much greater than the amount of fungus (Giordani, Padula, and Radice 2013), and the very low number of *T. deformans* peptides (54 maximum in G7C) detected by proteomic analysis in contrast to the high number of peptides (up to 1337 peptides) of *P. persica* origin in the same samples, metabolic changes described in both asymptomatic and symptomatic regions of PLCD-leaves can be attributed to signals from the leaves rather than to the fungus.

4.1 | Plastidic Functioning and Composition Is Altered in Symptomatic Areas

The downregulation of DAPs involved in chloroplastic protein biosynthesis and translocation systems in symptomatic areas may, in part, explain changes in the chloroplast proteome described in this work.

Photosynthetic functioning is undoubtedly declined in symptomatic areas. The decrease in different components of the photosynthetic machinery is accounted by a net decrease in chlorophylls a and b in G2C, G7C, G8C with respect to G0 (Figure 2), in different protein components of PSII, in the electron carrier plastocyanin and in the ATP synthase complex (Table S10). The reduction in chlorophylls in symptomatic areas were similar to those previously reported in completely curled leaves with respect to healthy ones (Moscatello et al. 2017).

Downregulation in enzymes of Calvin cycle is determined by differential proteomics and RuBisCO LSU Western blot (Figure 7 and Supporting Information S1: Figure S7, Table S10) and agrees with decreases in photorespiratory enzymes. As a consequence of reduction in CO_2 fixation, net decreases in exported photosynthates (sucrose and sorbitol), and in the storage of carbon (starch) in the chloroplasts are observed (Figure 3). Quantitative proteomics and Western blot analysis reveal both a drop in starch synthesis and an increase in its catabolism.

Diminishes in chlorophylls and RuBisCO are typical senescence markers, which are accompanied with protein and nucleic acids degradation that provides nutrients for not senescence organs. Leaf yellowing reveals the favoured chlorophyll catabolism over carotenoids in senescent leaves (Matile 1992). Here, downregulation of enzymes involved in protoporphyrin IX formation (M5X1B9, M5XBN6), Mg-chelation (M5WUE1) and cyclation (M5WCL2, Table S10) and in isoprenoid chain synthesis (Figure 8A), together with the absence of DAPs related to chlorophyll degradation, suggests a decrease in chlorophyll biosynthesis rather than a breakdown-activation. Moreover, in PLCD-leaves the decrease in the chlorophylls was not due to an increased chlorophyllase activity (Montalbini and Buonaurio 1986). Unlike the pattern observed in senescent leaves, carotenoids, usually associated with thylakoid membranes of PSI and PSII, decreased (Figure 2) in agreement with downregulation of plastidic carotenoid biosynthetic enzymes in G7C versus G0 (Figure 8A). Additionally, upregulation of

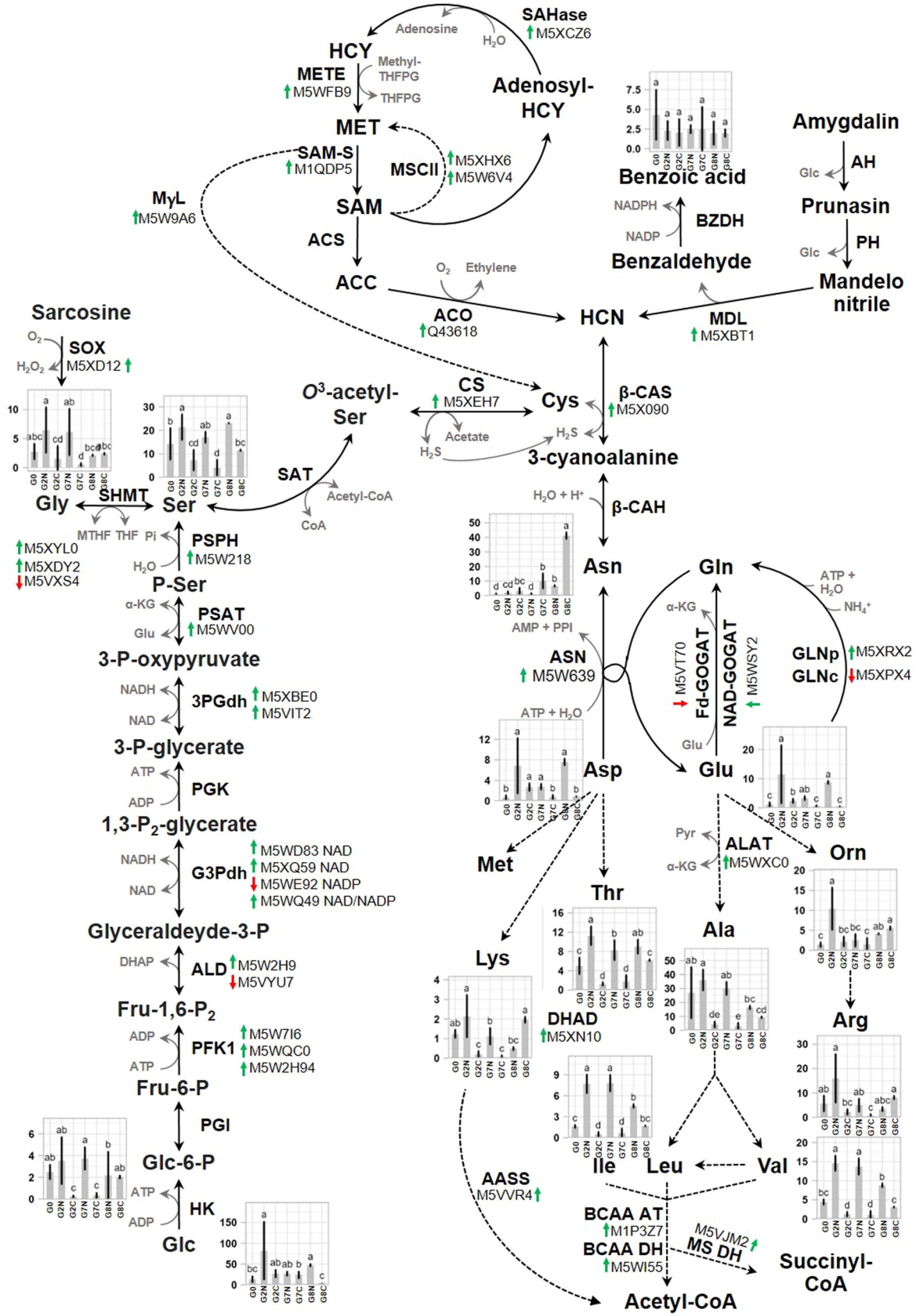

FIGURE 9 | Legend on next page.

carotenoid breakdown-related enzymes was not observed (Table S10). Moreover, enzymes involved in xanthophyll metabolism were also decreased in G7 versus G0 (Figure 8A). Together, these data indicate that a process different from senescence may be occurring in plastids of curled areas.

Transmission electron microscopy studies on areas exhibiting PLCD showed the spongy parenchyma cells had small and agranal chloroplasts lacking starch (Bassi, Conti, and Barbieri 1984). Main photosynthetic complexes are sub-compartmentalized in stacked and unstacked membrane regions in thylakoids. A great proportion of PSII and light harvesting complex II (LHCII) are located in the stacked grana core, while PSI and the LHCI, the remaining percentage of PSII and the ATPase complex are primarily concentrated in the margins of grana, the end of membranes and in the stroma lamellae (Albertsson 2001). In C_4 species such as maize, chloroplasts located in bundle sheath cells are fully agranal but completely functional (Yoshimura, Kubota, and Ueno 2004) and PSII is either completely absent or not all subunits of PSII are present (Sheen and Bogorad 1986; Bassi, Marquardt, and Lavergne 1995). Here, in G7C leaves, most of the decreased proteins with respect to G0 were related to either PSII assembly or maintenance. Components of PSI are not included in the DAPs list. Therefore, the differential photosynthetic protein composition of curled leaves areas fits with previously described changes in the chloroplast's structure (Bassi, Conti, and Barbieri 1984). In agreement with thylakoid rearrangement, three putative thylakoid lumenal predicted proteins were downregulated in G7C (M5W006, M5WDC5 and M5XKK0). Collectively, decreases in chlorophylls, carotenoids, PSII and LHCII components, plastocyanin and ATP synthase point towards a deficit in photophosphorylation due to decline electron transport in curled leaves rather than the operation of a cyclic pathway around PSI. Decreases in enzymes involved in chloroplast redox homoeostasis such as ferredoxin- (M5Y5H7) and NADPH-dependent thioredoxin reductases (TRX, M5W7R8, M5W964), M- (M5W0P5, M5WVD9, M5XQ68, M5W035) and X-type TRXs (M5XMF8) and a 2-Cys peroxiredoxin (2-CysPrx, M5W311); and changes in the saturation of TAGs are also indicative of alteration in the redox status of the plastids in G7C (Figures 4 and 5), with oxidated chloroplasts rather than over-reduced ones. Moreover, increase of OPPP enzymes suggests that in symptomatic areas NADPH is being generated outside the chloroplasts instead of by the photosynthetic electron transport chain.

Changes in the chloroplasts structure and composition are also evidenced at lipidome level (Figure 4). Particular lipid species are biochemical hallmark of different cellular compartments. In plastids, uncharged MGDGs and DGDGs are tightly bound to the reaction centres and represent the 80% of thylakoid lipids, while a 5%–12% is accounted by SQDG and a similar fraction by PG (Murata and Siegenthaler 1998; Loll et al. 2007). These galactolipids are also detected in the inner and outer envelope membranes but scarcely in other cell membranes (Block et al. 1983). Here, MGDGs, DGDGs and SQDGs positively correlated among each other (Supporting Information S1: Figure S5), in agreement with their co-localization in chloroplasts. MGDGs and DGDGs are non-bilayer and bilayer membrane forming lipids, due their capacity to destabilize or stabilize membranes, respectively (Hincha, Oliver, and Crowe 1998). In symptomatic areas, changes in these four lipid species are observed. SQDG 36:6 prominently decreases in G7C and G8C with respect to G0, respectively. Additionally, a significantly fall in symptomatic areas with respect to G0 is observed in DGDG 32:0, 34:6, 36:5 (2), 38:6 while MGDG 34:2, 34:5, 36:2, 36:3, 36:4, 36:5 and 38:6 show an increase (Figure 4 and Supporting Information S1: Figure S4, Table S4). Although it is difficult to predict the net impact of these changes inside plastids, it is clear the lipidome reconfiguration influences the photosynthetic machinery which organization differs in curled areas and in healthy leaves. The remodelling of membrane lipids is associated to diverse abiotic stresses in various plant species. A meta-analysis of 577 observations revealed that the abundance of MGDG and DGDG decreased when plants were exposed to different abiotic stresses (drought, temperature stress, salt stress, deficiency in nitrogen or Pi, aluminium and heavy mental stresses) (Liu et al. 2019). With respect to biotic stress, research has been focused in the role of lipids in signalling (Kachroo and Kachroo 2009). Nevertheless, lipidomic analyses are starting to emerge in this field. Li and Yu (2018) demonstrated a link between galactolipids and JA biosynthesis. Further they probed that an increase in MGDG:DGDG ratio is the primary cause of JA overproduction, as accounted by increased expression of LOXs, allene oxide synthase (AOS), and AOC involved in the JA biosynthesis (Yu, Lin, and Li 2020). It is accepted that JA biosynthesis starts after the release of fatty acids from the galactolipids of chloroplast membranes. Here, the modified ratio of MGDG:DGDG observed in symptomatic areas of PLCD and the upregulation of enzymes involved in a JA biosynthesis indicates that this hormone might be markedly elicited in symptomatic areas.

MGDGs and DGDGS tended to increase in asymptomatic tissues of PLCD-leaves. Moreover, MGDGs exhibited greater increases in G7N and G8N with respect to G0 than those of DGDGs, indicating an increase in MGDG/DGDG ratio which

FIGURE 9 | Scheme of amino acid and amino acid-related pathways in *P. persica*. ↑ and ↓ indicate the increase or decrease in the content of the protein in G7C with respect to G0, respectively. Bar charts show the relative levels of metabolites assessed by GC-MS in G0, G2N, G2C, G7N, G7C, G8N and G8C (from left to right). 3PGDH, 3-phosphoglycerate dehydrogenase; β-CAS, cyanoalanine synthase; AASS, alpha-aminoadipic semialdehyde synthase; ACO, 1-aminocyclopropane-1-carboxylate oxidase; AH, amygdalin hydrolase; ALD, aldolase; ASN, Asparagine synthetase; BCAA AT, branch chain amino acid aminotransferase; BCAA DH, BCCA dehydrogenase; BZDH, benzoic acid dehydrogenase; CAH, cyanoalanine hydratase; CS, cysteine synthase; GLN, Glutamine synthetase; HCY, homocysteine; MDL, R-mandelonitrile lyase; MET, 5-methyltetrahydropteroyltriglutamate-homocysteine S-methyltransferase; MγL, methionine γ lyase, MSCII, L-methionine salvage cycle 2; MSDH, methylmalonate-semialdehyde dehydrogenase; PFK-1, phosphofructokinase 1; PGK, phosphoglycerate kinase; PH, prunasin hydrolase; PSAT, phosphoserine aminotransferase; PSPH, phosphoserine hydrolase; SAHase, S-adenosylhomocysteinase; SAM-S, S-adenosylmethionine synthase; THFPG, tetrahydropteroyltri-L-glutamate. [Color figure can be viewed at wileyonlinelibrary.com]

could tend to the destabilization of membranes even in asymptomatic areas of sick leaves. Additionally, these changes affecting plastidic membranes may also affect chloroplastic protein translocation. Therefore, changes in MGDGs and DGDGs, which are markers of abiotic stress responses, could be considered as indicators of biotic stress in *P. persica*. On the other hand, while decreases in these lipid species are observed in response to abiotic effectors, increases are observed in *T. deformans* infected leaves (Liu et al. 2019).

While changes in lipidome are detected in G7N and G8N, modifications in the metabolome are less evident in asymptomatic areas of diseased leaves (Figures 3, 4, and 6). Therefore, lipids, like increases in individual MGDGs (34:1, 34:2, 34:3, 34:4, 34:5, 36:3, 36:4, 36:5, 36:6 and 38:6) or the overall amount of MGDG could act as more sensitive marker of infected tissue than metabolites or proteins in asymptomatic leaves.

4.2 | Amino Acid and Secondary Metabolism Are Altered in Symptomatic Areas of PLCD-Leaves

A remarkable feature of metabolomics conducted here is the modification in the pool of free amino acids, with a great increase in Asn in contrast to the decrease in the other amino acids (Figure 3A). Figure 9 depicts the pathways converging to Asn, deriving from Asp or from those starting from cyanogenic compounds and ethylene synthesis, which are connected with the metabolism of sulphur-containing amino acids and of serine and glycine.

In G7C leaves, not only Asn was increased (Figure 3, Table S1) with respect to G0 (12.6-fold) but also the enzymes involved in its synthesis from Asp (M5W639) and those related to glutamine synthesis (M5XRX2, M5WSY2). In addition, the change in Asn is more remarkable at G8C, with a 51.7-fold decrease with respect to G0. Asn may also come from HCN by the L-3-cyanoalanine synthase (β-CAS, M5X090) pathway. Moreover, two enzymes involved in HCN generation were upregulated in G7C with respect to G0, an R-mandelonitrile lyase (MDL, M5XBT1) and a 1-aminocyclopropane-1-carboxylate oxidase (ACO, Q43618); concomitantly with the increase in enzymes involved in SAM synthesis (M1QDP5, M5W6V4, M5XHX6, M5XCZ6, M5WFB9). Cyanogenic glucosides are specialized plant compounds that produce HCN. Amygdaline and prunasin are the main cyanogenic glucosides in fruits and in vegetative tissues (Sánchez-Pérez et al. 2008; Dicenta et al. 2002). Mandelonitrile, produced from prunasin, modified the response of *P. persica* seedlings against abiotic and biotic stress stimulus and modulated the salicylic acid content and the antioxidative metabolism (Bernal-Vicente et al. 2018, 2020). HCN is effective against pathogens such rice blast fungus (Gleadow and Møller 2014; Seo et al. 2011) and regulates different cellular processes (García et al. 2019). Here, proteomic data suggests an upregulation of this route in curled areas. Cysteine synthetase (CS, M5XEH7) was upregulated in symptomatic areas to form cysteine. Moreover, enzymes involved in Ser and 3-phosphoglycerate synthesis were also upregulated (Figure 9). According with their consumption to provide Cys, there was a decrease in Gly, Ser and in Glc-6-P in G7C with respect to G0 (Figure 3, Table S1).

Asn fulfils different roles in cellular homoeostasis. It is a protein component, participates in osmotic regulation, is a marker of protein synthesis inhibition and is the product of cyanogenic compounds detoxification (Loll et al. 2007). Asn and Gln are normally used for ammonium remobilization during protein catabolism in senescent leaves (Buchanan-Wollaston 1997). In areas with PLCD, besides the proteome reconfiguration, total protein content does not differ from that of heathy leaves (Figure 2) and there is a decrease in most of free amino acids rather than the typical increase observed in senescent leaves. Data obtained here suggest other role for Asn rather as a marker of leaf senescence and nitrogen mobilization. We previously showed that Asn was largely increased in leaves of the susceptible genotypes but not in the resistant one at 24 h post-inoculation, while the fungus was infecting and still in its yeast phase (Svetaz et al. 2017). *T. deformans* uses Asn as a nitrogen source (Mix 1935; Moore 2011) and its genome encodes an asparaginase. Thus, it was proposed that Asn could be used as substrate only very early after inoculation or acting as a signal to induce the dimorphism to the filamentous phase (Svetaz et al. 2017). Current results are indicative of Asn usage during the whole lifespan of the fungus, which manipulates plant metabolism to fulfil its nutritional demands when colonizing and when causing PLCD.

Proteomic analysis reveals secondary metabolism upregulation at terpenoid biosynthetic level in PLCD-leaves (Figure 8). Terpenoids include different compounds such as menthol, abscisic acid, chlorophyll, gibberellin and β-carotene and fulfil key roles in responses against biotic and abiotic stresses (Tholl, 2015). In symptomatic areas, enzymes of the mevalonate pathway NMRs were increased (Figure 8A, Table S3). NMR catalyzes the biosynthesis of neomenthol, a monoterpenoid, from menthone. NMR was increased in pepper against *Xhantomonas campestris* (Choi et al. 2008), in *Passiflora edulis* challenged with *X. axonopodis* (Munhoz et al. 2015) and in apple against *Alternaria alternata* (Ni et al. 2017). To the best of our knowledge, although encoded in the genome and identified in different works, NMRs have not been characterized in *P. persica* yet. Neomenthol occurrence has not been documented in this species, probably because volatilome analyses have been conducted mostly in fruits and under conditions in which this metabolite would not be induced, such as under a fungal attack. However, its precursor, limonene, has been found in *P. persica*. Moreover, neo-menthol has been identified in the volatilome of *P. domestica* (Thomazi-Kleina et al. 2021) revealing the presence of this compound in the *Prunus* genus. NMR was differentially accumulated between ripe and mature peach fruit (Nilo-Poyanco et al. 2021) and it was upregulated in roots of peach-almond hybrid rootstocks under Fe deficiency (Rodríguez-Celma et al. 2013). In *P. armeniaca*, a gene encoding a NMR was located in a QTL segment with cell growth regulatory genes and associated with kernel width (Zhang et al. 2023). Besides the role in plant defences, NMRs could be involved in cell hyperplasia and hypertrophy in PLCD-leaves. NMRs belong to the short-chain dehydrogenase/reductases of diverse functionality and could catalyze the synthesis of other metabolites different from neomenthol (Kallberg et al. 2002).

Enzymes involved in phenylpropanoid pathways were induced in PLCD areas (Figure 8B). The great decrease in Phe denotes

its increased consumption through this pathway (Figure 3, Supporting Information S1: Figure S2). Accumulation of anthocyanidin reductase (M5X6P6) agrees with the typical red coloration due to augmentation of anthocyanin levels in curled areas (Figure 2). Enzymes related to lignin precursors synthesis and peroxidases (M5W061, M5W6X8, M5W030) were also increased in G7C versus G0; in agreement with increased peroxidase activity measured in symptomatic leaves (Koleva-Valkova et al. 2017). In PLCD, enhanced lignification may contribute to leaf bending and cell strengthen. Ultrastructure analysis reveals partial degradation of mesophyll CWs; probably, due to cellulases and xylanases encoded in the pathogen genome (Piperkova and Vassilev 2023). The absence of lignin-degrading genes in the fungus genome (Cissé et al. 2013), together with enhanced lignification in the host, may explain the incomplete plant cell CW disruption of by *T. deformans*. Since total phenolics are not modified (Figure 2), decreases in Tyr and Phe (Figure 3) in curled areas might be compensated with increases in other phenolics like those shown in Figure 8. Besides lignin deposition and fungal enzymes action on plant CW, CW- remodelling is accounted by proteomic analysis showing the induction of proteins involved in hemicellulose and pectin metabolisms in symptomatic areas (Table S10) with enzymes involved in the synthesis (i.e., 1,4-β-glucan synthase) and others in the degradation (β-galactosidases, β-D-xylosidases and pectate lyase) or modification (xylan *O*-acetyltransferase, acetylxylan esterase and xyloglucan endotransglucosylase/hydrolase) of the CW. Moreover, mannose, which increases in G2C, G7C and G8N with respect to G0 (Figure 3) and xylose, which has a tendency to increase in symptomatic tissues, are sugars derived from the degradation of hemicellulose components such as mannans, xyloglucans and xylans and are indicative of changes in the plant CW structure.

One of the most remarkably symptoms of LPCD is leaf hyperplasia and hypertrophy, which have been suggested to occur due to increased cytokinin and auxin occurrence in the plant tissue (Yamada et al. 1990; Sziráki, Balázs, and Király 1975; Raggi 1995). Proteomics show the induction of the *P. persica* tryptophan aminotransferase (M5VM03) participating in the main route for auxin biosynthesis in plants (Casanova-Sáez, Mateo-Bonmatí, and Ljung 2021) and the modification in the level of auxin responsive proteins (Table S10). Metabolomics reveal the decrease in Trp (Figure 3) which can be used to produce indoleacetic acid. These data indicate that auxin is produced by the host in curled tissues and that this tissue is also showing a response to the hormone. Conversely, changes in the levels of proteins related to cytokinin metabolism or response have not been identified neither in G7C nor G7N with respect to G0. Although it cannot be ruled out that both hormones could be produced by the fungus, the lack of DAPs involved in cytokinin response in curled tissues suggest that changes in leaf anatomy are more likely to occur do to auxin action rather than cytokinins influence.

4.3 | Symptomatic Areas Resemble Sugar-Starved Leaves or Sink Tissues

Enzymes involved in both plastidic and cytosolic glycolysis, acetyl-CoA production and TCAC were increased in G7C with respect to G0. Therefore, carbohydrate oxidation through respiration would be covering the energetic demands not supplied by photosynthesis in diseased areas. The PEPC protein increase in G7C with respect to G0 (Table S10, Supporting Information S1: Figure S7) matches with rises in PEPC activity in infected tissue (Moscatello et al. 2017) and it indicates a re-fixation of CO_2 released by PDH and respiration, which is more compatible with a sink role of the infected areas.

Hypoxia is a frequent metabolic status under normal development (Ventura et al. 2020) and it is likely to occur in hyperplasic regions of leaves with PLCD where oxygen might be lowered due to reduced photosynthetic production. Thus, fermentative metabolism may also contribute to energy production through ADHs induction (Table S10). The role of ADH during pathogen infections has been accounted by inductions in kiwifruit crops infected with *Pseudomonas syringae* pv. *actinidiae* (Petriccione et al. 2013) and in barley against *Blumeria graminis* (Proels, Westermeier, and Hückelhoven 2011).

Hexose-sugars derived from photosynthesis, starch and imported photosynthates serve as the major energy substrates in plants. The degree of photosynthesis and of photoassimilate production are indicative of the role of a plant organ as a sink or as a source. Here, the main peach exported photosynthates, sucrose and sorbitol (Nadwodnik and Lohaus 2008), are decreased in symptomatic areas with respect to G0 (Figure 3). These changes are accompanied by an increase in sucrose catabolic enzymes and agrees with the reported increase in the activities of soluble invertases, sorbitol dehydrogenase and sucrose synthase in leaves with PLCD (Moscatello et al. 2017). These enzymes cooperate to maintain glucose and fructose similar to those of healthy leaves (Figure 3). In contrast, the decrease in Glc-6-P denotes its consumption through the glycolysis and OPPP (Figure 3). Collectively, symptomatic areas resemble sugar-starved leaves or sink tissues rather than source tissues (Figure 10).

Within a same leaf with PLCD, different groups of mesophyll cells might be functioning as a source and others as a sink, with the first ones providing assimilates to the hyperplasic and hypertrophic areas (Figure 10). The increase in protein content in asymptomatic areas with respect to G0 (Figure 2), with only very few DAPs (Figure 6), is indicative of an activation of metabolism in these cells probably due to the higher demand of assimilates of symptomatic areas (Figure 10). The greater the severity of the disease, the lower the ratio asymptomatic/symptomatic areas. This relationship explains the progressive decrease in starch in G2N, G7N and G8N (Figure 2), since hexoses produced by photosynthesis are used for sucrose and sorbitol synthesis rather than for starch accumulation. In mesophyll cells, the number of plasmodesmata was greater in PLCD than in noninfected leaves (Piperkova and Vassilev 2023). Symplastic transport of photoassimilates from healthy areas to diseased zones can be favoured by increased plasmodesmata and by their rapidly consumption to provide energy and to keep the concentration gradient from healthy to infected areas. Proteomic data did not reveal an increase in sugars transporters, supporting the increase in symplastic flow of sugars over the apoplastic one. In PLCD-asymptomatic areas (i.e., G2N) the relative levels of most of the miscellaneous compounds, organic acids and sugars, are similar to those of healthy leaves (G0),

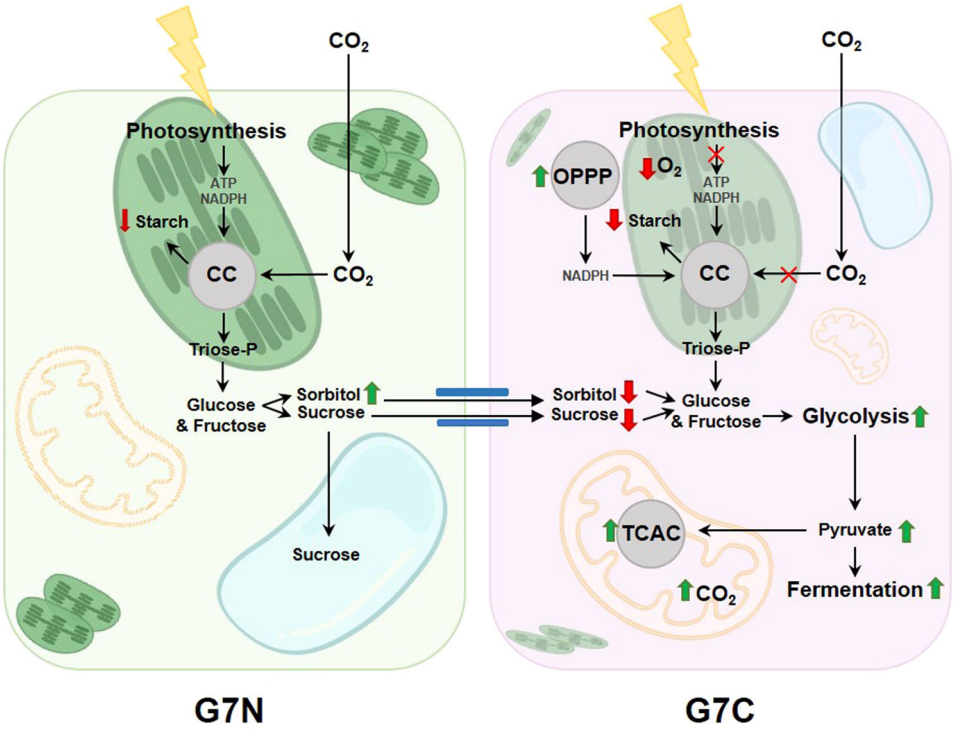

FIGURE 10 | Simplified scheme representing the metabolic changes in cells from asymptomatic and symptomatic areas of leaves with PLCD. CC, Calvin cycle; OPPP, pentose phosphate pathway; TCAC, tricarboxylic acid cycle. Plasmodesma is shown in blue. On the right, a typical cell of curled areas is represented. On the left, a mesophilic cell of asymptomatic areas from a leaf with PLCD is shown. [Color figure can be viewed at wileyonlinelibrary.com]

while Glu, Asp, Ile, Thr, Ser, Phe, Orn, Tyr, Val and β-Ala and total proteins are higher in G2N, G7N, and G7N with respect to G0 (Figure 2). Results presented here demonstrate that nitrogen metabolism is affected in both symptomatic and asymptomatic areas. In infected leaves the decrease in dry matter, which is in agreement with previous studies, was partially attributed to diminish in leaf nonstructural carbohydrates like sucrose, starch and sorbitol (Raggi 1994, Moscatello et al. 2017) also observed here (Figure 3). In peach leaves at different developmental stages, rises in photosynthesis, Calvin Cycle enzymes and carbohydrates correlated with increases in dry matter (Merlo and Passera 1991). Conversely, the less the photosynthesis, the less of the dry matter. The results on dissected symptomatic areas shown here also add evidence of the contribution of pigments, amino acids and organic acids in the dry matter decline and contribute to the understanding of the process underlying the decrease in photosynthesis in curled leaves.

4.4 | Triacylglycerols Are Differentially Accumulated and Peroxidated in PLCD-Leaves

One remarkable feature are the changes in TAGs species and total content in PLCD-leaves. In terms of total mass spectral signal, TAGs were accumulated in symptomatic areas with respect to asymptomatic areas and healthy leaves due to increases in TAGs with a low number of unsaturated bond (Figures 4 and 5, Table S4). Modification in the level of TAGs have been described in response to abiotic stress (Higashi and Saito 2019). However, the remodelling of lipid composition has been less studied in response to pathogens. In *Arabidopsis thaliana*, TAGs accumulated in leaves in response to elicitor, *Pseudomonas syringae* or *Verticillium longisporum* treatments (Schieferle et al. 2021) and also when exposed to an avirulent strain of *Pseudomonas syringae* (Zoeller et al. 2012). A role for TAGs in Arabidopsis defence has been proposed against *Colletotrichum higginsianum;* upon infection, TAGs accumulated in oil bodies to produce phytoalexins with antifungal activity from linolenic acid (Shimada et al. 2014). Conversely, in potato, *Phytophthora infestans* manipulates TAGs breakdown to evade host defences (Yang et al. 2021). Regarding the pathway contributing to TAG synthesis in symptomatic leaves, TAGs could be synthetized from pre-existing DAGs, which are decreased in symptomatic areas with respect to G0 (Figure 4). Besides the downregulation of a glycerol-3-phosphate acyltransferase (M5WM27, Table S10) found in G7C with respect to G0, *de novo* synthesis from an acyl-group and glycerol-3-phosphate cannot be ruled out due to decreases in their precursors hexadecenoic (C16, cis-9) and octadecanoic acids (C18) and glycerol-3-phosphate in symptomatic tissue with respect to G0 (Figures 3 and 4). Interestingly, the total mass spectral signal of TAGs in asymptomatic areas was decreased with respect to G0 (Figure 5). While most of the research in TAGs has been conducted in oil-seeds, less in known about TAG metabolism in leaves (Xu and Shanklin 2016). In leaves, TAGs are accumulated in plastoglobules in chloroplasts or as droplets in the cytosol. In asymptomatic tissue, besides photosynthesis is highly active to provide photosynthates to the symptomatic regions, in the same manner that starch is not accumulated due to exacerbated photosynthates exportation, the carbon and energy resources flux to storage lipids is decreased as well,

conducting to a decrease in the TAGs. In symptomatic areas, lipid peroxidation was demonstrated by TBARs increase (Figure 5C) which contributes to the decrease in the DBI (Figure 5B). Lipid peroxides can be generated by LOXs or by the attack of free radicals to the polyunsaturated fatty acids (Alché 2019). Here, increases in LOXs (M5W6C3, M5X5W8 and M5WJG6) in G7C with respect to G0 (Table S10) can contribute to lipid peroxidation. In addition, decreases in enzymes involved in the xanthophyll cycle (M5W4K8, M5VWI3 and M5W6E3), increases in peroxidases (M5W061, M5W6X8 and M5W030), accompanied by an imbalance of reactive oxygen species (ROS) synthesis and scavenging (like decreases in tocopherol, carotenoids, glutathione dehydrogenases M5X112 and M5WUW5, chloroplastic superoxide dismutase M5VZK2) can contribute to the production of ROS; and thus of lipid peroxidation in symptomatic areas.

4.5 | Stress Responsive Proteins Are Induced in PLCD-Leaves

The 34 DAPs identified in symptomatic areas belonged to nine of the 17 categories of PRs (van Loon, Rep, and Pieterse 2006). Most PRs but M5WAE7 (PR16), were upregulated in G7C versus G0 (Table S10). Six different PR16s were downregulated very early after inoculation in the apoplast fluid of leaves from *P. persica* either susceptible or resistant to *T. deformans* (Butassi, Novello, and Lara 2022) confirming that PR16 are not involved in the plant response to the pathogen. Other proteins such as M5X0X3 (PR2), M5WI79, M5X1P7, M5Y0J0 (PR3) and M5W1Q5 (PR4) were also upregulated in a susceptible genotype upon inoculation (Butassi, Novello, and Lara 2022). Other DAPs exclusively detected in the apoplast of the resistant genotype after inoculation like M5VM18, M5VQU4 (PR2), M5VQE4 (PR3), M5WA70, M5WR50, M5WT96, M5WTQ8, M5WV03 (PR5) and M5W030 (PR9) were also upregulated in G7C. Therefore, the timing of expression of some PRs might be crucial in fighting the fungus to conduct to the resistance, being early upregulated in a resistant genotype but also increased later when PLCD is established in the susceptible genotype. In addition, PR10 and PR5 were transcriptionally induced in both susceptible and resistant genotypes upon inoculation (Svetaz et al. 2017) and upregulated in the present work. PRs acting on pathogen CW (PR2, PR3 and PR4), peroxidases, PR5s and PR10s are not only early responsive proteins but also have a role during advanced stages of PLCD as it is the case of G7C. In contrast, PR12 (defensin) and PR17 exclusively induced in a resistant genotype after inoculation (Svetaz et al. 2017; Butassi, Novello, and Lara 2022) were not identified as DAPs neither in G7N nor G7C with respect to G0 (Table S10), supporting the hypothesis of their role in the resistance to PLCD.

5 | Conclusion

The metabolic processes in PLCD leaves were examined in both symptomatic and asymptomatic areas, revealing the profound changes in primary and secondary metabolism that are responsible for the leaf phenotype and performance which conduct to reduced productivity defoliation and tree death. Curled areas, in which photosynthesis is downregulated, function as sink tissue importing sugars and producing energy through fermentation and respiration, and reductive power from the OPPP. Symptomatic areas are characterized by an altered chloroplastic functioning and composition that includes decrease in the photosynthetic machinery, starch, carotenoid and chlorophyll biosynthesis and alteration in chloroplast redox homoeostasis proteins and lipids. Upregulation of phenylpropanoid and mevalonate pathways and downregulation of the plastidic methylerythritol phosphate route are observed in curled areas. The changes in amino acid pools and upregulation of proteins involved in asparagine synthesis in symptomatic areas may represent a host defence mechanism response or may be driven by the fungus for its growth. Proteomics reveals particular PRs accumulation in G7C, denoting the participation of these proteins not only in early defence events but also when the disease is established, indicating the accumulation of certain PRs are not sufficient to confer resistance to the disease.

This work reveals the importance of lipid metabolism in the interaction between *P. persica* and *T. deformans*. Lipidomics provides evidence of modification in the saturation of TAGs and points out lipids as early sensitive markers of PLCD in asymptomatic areas. Remodelling of the lipid composition of plastidic membranes alters photosynthetic machinery and affects the whole primary metabolism. Future studies comparing susceptible and resistant genotypes, focusing on lipidome changes after fungal inoculation, will clarify early lipid responses to the pathogen and distinguish between disease establishment and resistance mechanisms. Since chloroplasts play a central role in plant metabolism and defence and are highly affected in PLCD-leaves, research towards identifying fungal chloroplast-targeted effector will deepen our understanding in *P. persica-T. deformans* pathosystem.

Acknowledgements

Laura Andrea Svetaz, Claudia Anabel Bustamante, and María Valeria Lara are CONICET Researcher Career members. María Angelina Novello is a fellow of the same Institution. Claudia Anabel Bustamante received an Alexander von Humboldt Foundation fellowship at ARF lab. We thank Professors Bellini and Giordani (DISPAA, Università di Firenze) for *P. persica* selection.

This work was supported by Agencia Nacional de Promoción Científica y Tecnológica (PICT 2016-0819).

Conflicts of Interest

The authors declare no conflicts of interest.

DATA AVAILABILITY STATEMENT

The data that supports the findings of this study are available in the supplementary material of this article.

References

Agrios, G. 2005. *Plant Pathology* (5th Edition). Burlington, MA, USA: Elsevier Academic Press.

Albertsson, P. Å. 2001. "A Quantitative Model of the Domain Structure of the Photosynthetic Membrane." *Trends in Plant Science* 6: 349–354.

Alché, J. D. 2019. "A Concise Appraisal of Lipid Oxidation and Lipoxidation in Higher Plants." *Redox Biology* 23: 101136.

Bassi, M., G. G. Conti, and N. Barbieri. 1984. "Cell Wall Degradation by *Taphrina deformans* in Host Leaf Cells." *Mycopathologia* 88: 115–125.

Bassi, R., J. Marquardt, and J. Lavergne. 1995. "Biochemical and Functional Properties of Photosystem II in Agranal Membranes From Maize Mesophyll and Bundle Sheath Chloroplasts." *European Journal of Biochemistry* 233: 709–719.

Bellini, E., E. Giordani, R. Perria, and D. Paffetti. 2002. "Leaf Curl in Peach: New Resistant Genotypes and Molecular Markers." In *ISHS Acta Horticulturae*, edited by R. S. V International Peach Symposium Johnson and C. H. Crisosto (592, 649–653).

Bernal-Vicente, A., D. Cantabella, J. A. Hernández, and P. Diaz-Vivancos. 2018. "The Effect of Mandelonitrile, a Recently Described Salicylic Acid Precursor, on Peach Plant Response Against Abiotic and Biotic Stresses." *Plant Biology* 20: 986–994.

Bernal-Vicente, A., C. Petri, J. A. Hernández, and P. Diaz-Vivancos. 2020. "Biochemical Study of the Effect of Stress Conditions on the Mandelonitrile-Associated Salicylic Acid Biosynthesis in Peach." *Plant Biology* 22: 277–286.

Block, M. A., A. J. Dorne, J. Joyard, and R. Douce. 1983. "Preparation and Characterization of Membrane Fractions Enriched in Outer and Inner Envelope Membranes From Spinach Chloroplasts. II. Biochemical Characterization." *Journal of Biological Chemistry* 258: 13281–13286.

Borsani, J., C. O. Budde, L. Porrini, et al. 2009. "Carbon Metabolism of Peach Fruit After Harvest: Changes in Enzymes Involved in Organic Acid and Sugar Level Modifications." *Journal of Experimental Botany* 60: 1823–1837.

Buchanan-Wollaston, V. 1997. "The Molecular Biology of Leaf Senescence." *Journal of Experimental Botany* 48: 181–199.

Bustamante, C. A., Y. Brotman, L. L. Monti, et al. 2018. "Differential Lipidome Remodeling During Postharvest of Peach Varieties With Different Susceptibility to Chilling Injury." *Physiologia Plantarum* 163: 2–17.

Butassi, E., M. A. Novello, and M. V. Lara. 2022. "*Prunus persica* Apoplastic Proteome Analysis Reveals Candidate Proteins Involved in the Resistance and Defense Against *Taphrina deformans*." *Journal of Plant Physiology* 276: 153780.

Cantín, C. M., M. A. Moreno, and Y. Gogorcena. 2009. "Evaluation of the Antioxidant Capacity." *Journal of Agricultural and Food Chemistry* 57: 4586–4592.

Casanova-Sáez, R., E. Mateo-Bonmatí, and K. Ljung. 2021. "Auxin Metabolism in Plants." *Cold Spring Harbor Perspectives in Biology* 13, no. 3: a039867.

Choi, H. W., B. G. Lee, N. H. Kim, et al. 2008. "A Role for a Menthone Reductase in Resistance Against Microbial Pathogens in Plants." *Plant Physiology* 148: 383–401.

Cimen, I., and B. B. Ertugrul. 2007. "Determination of Mycoflora in Almond Plantations Under Drought Conditions in Southeastern Anatolia Project Region, Turkey." *Plant Pathology Journal* 6: 82–86.

Cissé, O. H., J. M. Almeida, A. Fonseca, et al. 2013. "Genome Sequencing of the Plant Pathogen Taphrina Deformans, the Causal Agent of Peach Leaf Curl." *mBio* 4, no. 3: e00055.

Colombo, S. L., C. S. Andreo, and R. Chollet. 1998. "The Interaction of Shikimic Acid and Protein Phosphorylation With PEP Carboxylase From the C_4 Dicot *Amaranthus viridis*." *Phytochemistry* 48: 55–59.

Dicenta, F., P. Martínez-Gómez, N. Grané, et al. 2002. "Relationship Between Cyanogenic Compounds in Kernels, Leaves, and Roots of Sweet and Bitter Kernelled Almonds." *Journal of Agricultural and Food Chemistry* 50: 2149–2152.

Fernie, A. R., A. Aharoni, L. Willmitzer, et al. 2011. "Recommendations for Reporting Metabolite Data." *Plant Cell* 23: 2477–2482.

Fonseca, A., and M. G. Rodrigues. 2011. "*Taphrina Fries*, Chapter 73." In *The Yeasts, a Taxonomic Study*, edited by C. P. Kurtzman, W. Jack, J. W. Fell, and T. Boekhout, 823–858. The Netherlands: Elsevier.

García, I., L. Arenas-Alfonseca, I. Moreno, C. Gotor, and L. C. Romero. 2019. "HCN Regulates Cellular Processes Through Posttranslational Modification of Proteins by *S*-Cyanylation." *Plant Physiology* 179: 107–123.

Giordani, E., G. Padula, and S. Radice. 2013. "Compared Anatomy of Young Leaves of *Prunus persica* (L.) Batsch With Different Degrees of Susceptibility to *Taphrina deformans* (Berk.) Tul." *Journal of Phytopathology* 161: 190–196.

Gleadow, R. M., and R. B. L. Møller. 2014. "Cyanogenic Glycosides: Synthesis, Physiology, and Phenotypic Plasticity." *Annual Review of Plant Biology* 65: 155–185.

Goldy, C., L. A. Svetaz, C. A. Bustamante, et al. 2017. "Comparative Proteomic and Metabolomic Studies Between *Prunus persica* Genotypes Resistant and Susceptible to *Taphrina deformans* Suggest a Molecular Basis of Resistance." *Plant Physiology and Biochemistry* 118: 245–255.

Higashi, Y., and K. Saito. 2019. "Lipidomic Studies of Membrane Glycerolipids in Plant Leaves Under Heat Stress." *Progress in Lipid Research* 75: 100990.

Hincha, D. K., A. E. Oliver, and J. H. Crowe. 1998. "The Effects of Chloroplast Lipids on the Stability of Liposomes During Freezing and Drying." *Biochimica et Biophysica Acta (BBA) - Biomembranes* 1368, no. 1: 150–160.

Kachroo, A., and P. Kachroo. 2009. "Fatty Acid-Derived Signals in Plant Defense." *Annual Review of Phytopathology* 47: 153–176.

Kallberg, Y., U. Oppermann, H. Jörnvall, and B. Persson. 2002. "Short-Chain Dehydrogenases/Reductases (SDRS): Coenzyme-Based Functional Assignments in Completed Genomes." *European Journal of Biochemistry* 269: 4409–4417.

Koleva-Valkova, L., N. Piperkova, V. Petrov, and A. Vassilev. 2017. "Biochemical Responses of Peach Leaves Infected With *Taphrina deformans* Brek/Tul." *Acta Universitatis Agriculturae et Silviculturae Mendelianae Burnensis* 65: 90.

Kopka, J., N. Schauer, S. Krueger, et al. 2005. "GMD@CSB.DB: The Golm Metabolome Database." *Bioinformatics* 21: 1635–1638.

Laemmli, U. K. 1970. "Cleavage of Structural Proteins During the Assembly of the Head of Bacteriophage T4." *Nature* 227: 680–685.

Lara, M. V., C. Bonghi, F. Famiani, G. Vizzotto, R. P. Walker, and M. F. Drincovich. 2020. "Stone Fruit as Biofactories of Phytochemicals With Potential Roles in Human Nutrition and Health." *Frontiers in Plant Science* 11: 562252.

Li, H., and C.-W. Yu. 2018. "Chloroplast Galactolipids: The Link Between Photosynthesis, Chloroplast Shape, Jasmonates, Phosphate Starvation and Freezing Tolerance." *Plant and Cell Physiology* 59: 1128–1134.

Liu, X., D. Ma, Z. Zhang, et al. 2019. "Plant Lipid Remodeling in Response to Abiotic Stresses." *Environmental and Experimental Botany* 165: 174–184.

Loll, B., J. Kern, W. Saenger, A. Zouni, and J. Biesiadka. 2007. "Lipids in Photosystem II: Interactions With Protein and Cofactors." *Biochimica et Biophysica Acta (BBA)—Bioenergetics* 1767: 509–519.

van Loon, L. C., M. Rep, and C. M. J. Pieterse. 2006. "Significance of Inducible Defense-Related Proteins in Infected Plants." *Annual Review of Phytopathology* 44: 135–162.

Matile, P. 1992. "Chloroplast Senescence." In *Crop Photosynthesis: Spatial and Temporal Determinants*, edited by N. R. Baker and H. Thomas, 413–440. Amsterdam: Elsevier.

Merlo, L., and C. Passera. 1991. "Changes in Carbohydrate and Enzyme Levels During Development of Leaves of *Prunus persica*, a Sorbitol Synthesizing Species." *Physiologia Plantarum* 83: 621–626.

Mix, A. J. 1935. "The Life History and Cytology of *Taphrina deformans*." *Phytopathology* 25: 41–66.

Montalbini, P., and R. Buonaurio. 1986. "Chlorophyllase Activity and Chlorophyll Content of Peach Leaves (c.v. 'Red Haven') During the Infection With *Taphrina deformans* (Berk.)Tul." *Rivista di Patologia Vegetale* 4: 23–29.

Monti, L. L., C. A. Bustamante, S. Osorio, et al. 2016. "Metabolic Profiling of a Range of Peach Fruit Varieties Reveals High Metabolic Diversity and Commonalities and Differences During Ripening." *Food Chemistry* 190: 879–888.

Moore, R. T. 2011. *Lalaria. In The Yeasts: A Taxonomic Study*, edited by C. Kurtzman, J. W. Fell, and T. Boekhout, (Fifth ed, 582–591). Elsevier.

Moscatello, S., S. Proietti, R. Buonaurio, et al. 2017. "Peach Leaf Curl Disease Shifts Sugar Metabolism in Severely Infected Leaves From Source to Sink." *Plant Physiology and Biochemistry* 112: 9–18.

Munhoz, C. F., A. A. Santos, R. A. Arenhart, L. Santini, C. B. Monteiro-Vitorello, and M. L. C. Vieira. 2015. "Analysis of Plant Gene Expression During Passion Fruit-Xanthomonas Axonopodis Interaction Implicates Lipoxygenase 2 in Host Defence." *Annals of Applied Biology* 167: 135–155.

Murata, N., and P.-A. Siegenthaler. 1998. "Lipids in Photosynthesis: An Overview." In *Lipids in Photosynthesis: Structure, Function and Genetics*, edited by P.-A. Siegenthaler and N. Murata, 1–20. Dordrecht, The Netherlands: Kluwer Academic Publishers.

Nadwodnik, J., and G. Lohaus. 2008. "Subcellular Concentrations of Sugar Alcohols and Sugars in Relation to Phloem Translocation in *Plantago major*, *Plantago maritima*, *Prunus persica*, and *Apium graveolens*." *Planta* 227: 1079–1089.

Ni, W., L. Zhu, R. Sha, J. Tao, B. Cai, and S. Wang. 2017. "Comparative iTRAQ Proteomic Profiling of Susceptible and Resistant Apple Cultivars Infected by Alternaria Alternata Apple Pathotype." *Tree Genetics and Genomes* 13: 23.

Nilo-Poyanco, R., C. Moraga, G. Benedetto, A. Orellana, and A. M. Almeida. 2021. "Shotgun Proteomics of Peach Fruit Reveals Major Metabolic Pathways Associated to Ripening." *BMC Genomics* 22: 17.

Peralta, D. A., A. Araya, M. V. Busi, and D. F. Gomez-Casati. 2016. "The E3 Ubiquitin-Ligase SEVEN IN ABSENTIA Like 7 Mono-Ubiquitinates Glyceraldehyde-3-Phosphate Dehydrogenase 1 Isoform in Vitro and Is Required for Its Nuclear Localization in *Arabidopsis thaliana*." *International Journal of Biochemistry & Cell Biology* 70: 48–56.

Petriccione, M., I. Di Cecco, S. Arena, A. Scaloni, and M. Scortichini. 2013. "Proteomic Changes in *Actinidia Chinensis* Shoot During Systemic Infection With a Pandemic *Pseudomonas syringae* pv. Actinidiae Strain." *Journal of Proteomics* 78: 461–476.

Piperkova, N., and A. Vassilev. 2023. "Ultrastructural Changes in Mesophyll Cells in Peach Leaves Infected by *Taphrina deformans* (Berk/Tul)." *Acta Agrobotanica* 76: 172969.

Proels, R. K., W. Westermeier, and R. Hückelhoven. 2011. "Infection of Barley With the Parasitic Fungus *Blumeria graminis* f.sp. *hordei* Results in the Induction of *Hvadh1* and *HvADH2*." *Plant Signaling & Behavior* 6, no. 10: 1584–1587.

Raggi, V. 1994. "Gas Exchange and Carbon Balance in Peach Leaves Infected by *Taphrina deformans*." *Plant Science* 98: 117–126.

Raggi, V. 1995. "CO2assimilation, Respiration and Chlorophyll Fluorescence in Peach Leaves Infected Bytaphrina Deformans." *Physiologia Plantarum* 93: 540–544.

Righini, S., E. J. Rodriguez, C. Berosich, E. Grotewold, P. Casati, and M. L. Falcone Ferreyra. 2019. "Apigenin Produced By Maize Flavone Synthase I and II Protects Plants Against UV-B-Induced Damage." *Plant Cell & Environment* 42: 495–508.

Ritchie, D. F. 1981. "Susceptibility and Inheritance of Susceptibility to Peach Leaf Curl in Peach and Nectarine Cultivars." *Plant Disease* 65: 731–734.

Rodríguez-Celma, J., G. Lattanzio, S. Jiménez, et al. 2013. "Changes Induced by Fe Deficiency and Fe Resupply in the Root Protein Profile of a Peach-Almond Hybrid Rootstock." *Journal of Proteome Research* 12: 1162–1172.

Roessner-Tunali, U., B. Hegemann, A. Lytovchenko, et al. 2003. "Metabolic Profiling of Transgenic Tomato Plants Overexpressing Hexokinase Reveals That the Influence of Hexose Phosphorylation Diminishes During Fruit Development." *Plant Physiology* 133: 84–99.

Rossi, V., M. Bolognesi, and S. Giosuè. 2007. "Influence of Weather Conditions on Infection of Peach Fruit by *Taphrina deformans*." *Phytopathology®* 97: 1625–1633.

Rossi, V., M. Bolognesi, L. Languasco, and S. Giosuè. 2006. "Influence of Environmental Conditions on Infection of Peach Shoots by *Taphrina deformans*." *Phytopathology®* 96: 155–163.

Rossi, V., and L. Languasco. 2007. "Influence of Environmental Conditions on Spore Production and Budding in *Taphrina deformans*, the Causal Agent of Peach Leaf Curl." *Phytopathology®* 97: 359–365.

Saeed, A. I., V. Sharov, J. White, et al. 2003. "TM4: A Free, Open-Source System for Microarray Data Management and Analysis." *Biotechniques* 34: 374–378.

Sánchez-Pérez, R., K. Jørgensen, C. E. Olsen, F. Dicenta, and B. L. Møller. 2008. "Bitterness in Almonds." *Plant Physiology* 146: 1040–1052.

Schieferle, S., B. Tappe, P. Korte, M. J. Mueller, and S. Berger. 2021. "Pathogens and Elicitors Induce Local and Systemic Changes in Triacylglycerol Metabolism in Roots and in Leaves of *Arabidopsis thaliana*." *Biology* 10: 920.

Schwacke, R., G. Y. Ponce-Soto, K. Krause, et al. 2019. "MapMan4: A Refined Protein Classification and Annotation Framework Applicable to Multi-Omics Data Analysis." *Molecular Plant* 12, no. 6: 879–892.

Seo, S., I. Mitsuhara, J. Feng, T. Iwai, M. Hasegawa, and Y. Ohashi. 2011. "Cyanide, a Coproduct of Plant Hormone Ethylene Biosynthesis, Contributes to the Resistance of Rice to Blast Fungus." *Plant Physiology* 155: 502–514.

Sheen, J. Y., and L. Bogorad. 1986. "Differential Expression of Six Light-Harvesting Chlorophyll a/b Binding Protein Genes in Maize Leaf Cell Types." *Proceedings of the National Academy of Sciences* 83: 7811–7815.

Shimada, T. L., Y. Takano, T. Shimada, et al. 2014. "Leaf Oil Body Functions as a Subcellular Factory for the Production of a Phytoalexin in Arabidopsis." *Plant Physiology* 164: 105–118.

Svetaz, L. A., C. A. Bustamante, C. Goldy, et al. 2017. "Unravelling Early Events in the *Taphrina deformans–Prunus persica* Interaction: An Insight Into the Differential Responses in Resistant and Susceptible Genotypes." *Plant, Cell & Environment* 40: 1456–1473.

Sziráki, I., E. Balázs, and Z. Király. 1975. "Increased Levels of Cytokinin and Indoleacetic Acid in Peach Leaves Infected With *Taphrina deformans*." *Physiological Plant Pathology* 5: 45–50.

Tholl, D. 2015. "Biosynthesis and Biological Functions of Terpenoids in Plants." *Advances in Biochemical Engineering/Biotechnology* 148: 63–106.

Thomazi-Kleina, H., M. J. Ballesteros Garcia, T. Oliveira De Melo, M. A. Dalbó, F. D. A. Marques, and L. L. May-De-Mio. 2021. "Volatile Compounds From Plum Genotypes With Different Levels of Resistance to Leaf Scald Disease." *Plant Pathology* 70: 1850–1859.

Tyanova, S., T. Temu, P. Sinitcyn, et al. 2016. "The Perseus Computational Platform for Comprehensive Analysis of (Prote)Omics Data." *Nature Methods* 13: 731–740.

Ventura, I., L. Brunello, S. Iacopino, et al. 2020. "Arabidopsis Phenotyping Reveals the Importance of Alcohol Dehydrogenase and Pyruvate Decarboxylase for Aerobic Plant Growth." *Scientific Reports* 10: 16669.

Wintermans, J. F. G. M., and A. De Mots. 1965. "Spectrophotometric Characteristics of Chlorophylls a and b and Their Phenophytins in Ethanol." *Biochimica et Biophysica Acta (BBA) - Biophysics Including Photosynthesis* 109: 448–453.

Xu, C., and J. Shanklin. 2016. "Triacylglycerol Metabolism, Function, and Accumulation in Plant Vegetative Tissues." *Annual Review of Plant Biology* 67: 179–206.

Yamada, T., H. Tsukamoto, T. Shiraishi, T. Nomura, and H. Oku. 1990. "Detection of Indoleacetic Acid Biosynthesis in Some Species of Taphrina Causing Hyperplastic Diseases in Plants." *Japanese Journal of Phytopathology* 56: 532–540.

Yang, L.-N., H. Liu, Y.-P. Wang, et al. 2021. "Pathogen-Mediated Stomatal Opening: A Previously Overlooked Pathogenicity Strategy in the Oomycete Pathogen *Phytophthora infestans*." *Frontiers in Plant Science* 12: 668797.

Yoshimura, Y., F. Kubota, and O. Ueno. 2004. "Structural and Biochemical Bases of Photorespiration in C_4 Plants: Quantification of Organelles and Glycine Decarboxylase." *Planta* 220: 307–317.

Yu, C.-W., Y.-T. Lin, and H. Li. 2020. "Increased Ratio of Galactolipid MGDG: DGDG Induces Jasmonic Acid Overproduction and Changes Chloroplast Shape." *New Phytologist* 228: 1327–1335.

Zhang, Q., Y. Zhang, W. Liu, et al. 2023. "Re-Sequencing and Morphological Data Revealed the Genetics of Stone Shell and Kernel Traits in Apricot." *Frontiers in Plant Science* 14: 1196754.

Zoeller, M., N. Stingl, M. Krischke, et al. 2012. "Lipid Profiling of the Arabidopsis Hypersensitive Response Reveals Specific Lipid Peroxidation and Fragmentation Processes: Biogenesis of Pimelic and Azelaic Acid." *Plant Physiology* 160: 365–378.

Supporting Information

Additional supporting information can be found online in the Supporting Information section.